Assessment of Panel and Vortex Particle Methods for the Modelling of Stationary Propeller Wake Wash

by

© Evan H. Martin

A thesis submitted to the

School of Graduate Studies

in partial fulfilment of the

requirements for the degree of

Master of Engineering

Department of Engineering and Applied Science

Memorial University of Newfoundland

October 2015

St. John's Newfoundland

Abstract

Icebreakers equipped with azimuth thrusters are becoming more common due to the tremendous operational benefits they provide. Despite the operational experience that exists, little is understood about the ability to break or clear ice using propeller wake.

Naval architects who wish to design vessels to exploit this phenomenon currently have no verified methods of determining the effectiveness of their design decisions. Hence, it is extremely difficult to justify novel icebreaker design concepts where the mission profile includes breaking ice with propeller wake.

This thesis explores the technical feasibility of using the panel method to model the hydrodynamic characteristics of the wake such that it could be applied to the problem of breaking and clearing ice using the wake from propellers. The scope of the research includes coupled vortex particle methods to overcome the difficulties encountered with panel methods.

Acknowledgements

I would like to sincerely thank all those who provided support throughout my graduate studies. This includes those whom provided financial, technical, as well as moral support.

Specifically, I would like to thank Dr. Brian Veitch, for providing direct supervision of my graduate studies. His guidance on both academic and professional matters not only shaped this thesis, but also my professional advancement as a whole. Acknowledgement is given to my co-supervisor Dr. Wei Qiu, for providing technical assistance in the area of panel methods.

Gratitude is extended to Dr. Arno Keinonen of AKAC Inc for both industrial guidance and financial support throughout the duration of my degree. My work with AKAC provided the inspiration for this research and engaged my interest to the ice offshore industry as a whole. The ability to witness ice breaking using azimuth thrusters in full scale helped shape this work by developing a practical understanding of the challenges faced by the industry.

Additional financial support was also provided by Memorial University and the Research and Development Corporation of Newfoundland and Labrador through an RDC Ocean Industries Research Award. This support is greatly appreciated.

Thanks also to my colleagues, family, and friends, for providing moral support. Specifically, Trevor Harris and Tyler Cole for reviewing draft versions of this thesis. Most importantly, my wife Deanna who has supported me throughout this journey.

To all those who provided support, either directly or indirectly, thank you.

Contents

List of Tables

List of Figures

Nomenclature

Symbols

Γ	Potential jump across wake surface
μ	Dipole strength
Φ	Irrotational scalar fluid velocity potential
ρ	Fluid density
σ	Source strength
α	Vortex particle strength
$\vec{\Omega}$	Rotational velocity of body
$\vec{\omega}$	Fluid vorticity
$\vec{\Psi}$	Rotational vector fluid velocity potential
$\delta(x)$	Dirac Delta function
A	Area of panel element
H	Gradient of the green's function
N	Number of elements
r_c	Vortex particle core radius
W	Gradient of the green's function when applied to wake panels
G	Three dimensional Greens function

$\hat{i}$, $\hat{j}$, $\hat{k}$ Unit cartesian coordinate vectors in global coordinate frame

$\vec{K}(\vec{r})$ Vortex particle vorticity kernel

$\hat{n}$ Unit normal vector to boundary surface (pointing into fluid domain)

P Pressure

$Q(\rho)$ Vortex particle regularization function

$\vec{r}$ Position vector in global reference frame

S Boundary Surface

S' Boundary surface excluding singularity

$\vec{T}$ Location of panel nodes in global coordinates

$\vec{U}$ Fluid velocity

$\vec{V}$ Velocity of rigid body

V Fluid domain

Subscripts

∞ Far field

c Panel centroid

B Propeller

b Body panel element

f Fluid domain

G Propeller's centre of gravity

I Ice

k Vortex particle

l, u Lower and upper wake boundary surfaces

p, q Points on boundary surface

q' Mirror of point q about plane defined by $z = 0$

v	Wake panel element within a strip w
W	Wake
w	Strip of wake panel elements
x,y,z	Cartesian coordinates in global coordinate frame

Chapter 1

Introduction

In the last 20 years, icebreaking operations have been revolutionized by the introduction of azimuth thrusters. Propeller wake is extremely powerful and thus has the ability to break sea ice. Azimuth thrusters have enabled new types of icebreaking operations by allowing the propellers to be continuously rotated. Hence, the wake can be intentionally directed towards the ice to provide efficient icebreaking operations.

This new type of icebreaking has brought many practical benefits to a variety of marine operations. Despite the large number of icebreakers currently equipped with azimuth thrusters, and the operational benefits that are being realized, there is little known about the efficiency of breaking and clearing ice using propeller wake. Only limited full scale data has been collected, and the only known published data is from the full scale trials of the MSV Fennica and MSV Botnica [32, 42]. Martin has developed a semi-empirical model based on these results in addition to unpublished data [35]. Additionally, Ferrieri has performed a systematic series of model tests to estimate the ability of propeller wake to clear ice floes [13].

This work has been motivated by previous work of the author [35] and the desire to use approaches that more accurately reflect the physical nature of the problem. The purpose of this thesis is to assess the technical feasibility of using the panel method to predict the hydrodynamic characteristics of the wake such that it could be applied to the problem of breaking and clearing ice using the wake from propellers. The panel method was selected for this work for two reasons:

- It is considered highly desirable to avoid a grid in the fluid domain, as required by CFD methods, due to the complex geometry of the propeller. The discretization of a grid in the fluid domain would need to be redeveloped each time step due to the relative motion between the propeller and ice surfaces. The panel method overcomes this complexity by allowing the grid to be limited to the surface of the bodies. The grids can be created for each body in a body fixed coordinate system and related to a global coordinate system based on the bodies' position and orientation.

- The panel method has seen widespread use in propeller design applications. Hence, an extension of the panel method would allow design features to be incorporated directly into the model. Approaches that do not explicitly model the propeller may not adequately capture the influence of the propeller design. Hence, this approach would provide designers a better understanding of the influence of design choices on the operational capabilities associated with breaking ice using the wake.

Chapter 2 provides background to the motivation for this work. Azimuth icebreakers are introduced both in terms of their operational benefits and current design

challenges. Some full scale data are presented that highlight the future application of this work, and emphasize some of the phenomenon that a successful approach should be capable of explaining. The history of panel methods is also briefly presented in this chapter.

Chapter 3 describes the theory used in the development of the propeller panel method. The theory is then expanded into a numerical approach in Chapter 4. The chapter ends by summarizing the fundamental challenges encountered while attempting to model the downstream propeller wake. Chapter 5 introduces Vortex Particle Methods as an alternative approach to model the propeller wake, and explains how it has been coupled to the panel method developed in Chapters 3 and 4.

Finally, Chapter 6 presents some numerical examples demonstrating the capabilities of the numerical model that has been developed for this work. The examples include basic validation using a sphere and a vortex ring. More complex examples using wings are then presented. Finally, the model is applied to a B-Series propeller. This is followed by a discussion of the challenges encountered and potential solution in Chapter 7. The thesis is then concluded and recommendations are presented for further developing the approach established by this work.

Chapter 2

Background

2.1 Azimuth Icebreakers

The use of azimuth thrusters in ice can be traced back as far the terminal tugs Aulis, Kari, and Esko built for Neste Oil in Finland during the 1980's [49]. However, it was not until the construction of the MSV Fennica in 1993 that azimuth thrusters were first introduced on icebreakers [32]. At the time, the full range of benefits that azimuth thrusters brought to various operations were not recognized. Although observed to a limited extent during the ice model tests, it was not until the full-scale trials of the Fennica in 1993 that the potential of the propeller wake as a means of icebreaking was fully realized. Since the construction of the Fennica, the operational benefits of using azimuth thrusters have become more widely understood. This has resulted in more icebreakers being designed and built with azimuth thrusters. These icebreakers have varied in their missions; ranging from escort vessels, offshore support vessels, and science vessels. Some recent icebreakers equipped with azimuthal thrusters include

the MSV Botnica, USCG Great Lakes Icebreaker Mackinaw, SCF Sakhalin, MV Pacific Enterprise, and most recently the RV Sikuliaq. There are also a number of ice capable tugs designed with azimuth thrusters including Neste Oil's terminal tug Ahti, and Sakhalin Energy's terminal tug Svitzer Sakhalin (and sisterships), to name just a few.

The author has had the opportunity to witness the application of propeller wake on icebreaking first hand on a variety of occasions:

- MSV Fennica – Gulf of Bothnia (2007)
- Terminal tug Ahti – Espoo Finland (2007)
- Svitzer Sakhalin – Sakhalin (2007)
- Pacific Endeavour – Sakhalin (2007)
- MSV Fennica – Fram Strait (2009)
- RV Sikuliaq – Bering Sea (2015)

Much of the information presented here is based upon these experiences.

2.2 Operational Benefits of Azimuth Icebreakers

The major advantage of utilizing azimuth thrusters is the ability to break and clear ice using the propeller wake, while orientating the wake in a variety of directions. This allows for entirely new approaches to icebreaking compared to traditional propulsion arrangements, where it was not possible to direct the wake, other than to a very

limited extent by the rudder. This new ability has improved the efficiency of certain operations, and has even enabled operations never before possible.

One significant benefit of azimuth thrusters on icebreakers is increased manoeuvrability. Not only can azimuth thrusters provide increased turning moment, but also the ability to break ice with the wake allows azimuth icebreakers to be turned on the spot, even in the presence of ice. By orientating the wake outboard, a large enough area of ice can be broken such that the vessel can turn around in the area of open water created.

Another benefit is the ability to orient the wake outboard while icebreaking. This technique allows the wake to break ice to the sides of the vessel, while still maintaining forward progress. This has the effect of creating a channel wider than the icebreaker, while also leaving fewer floes in the channel [32]. This has practical applications in a variety of fields. Escort operations can use this technique to reduce resistance on the escorted vessel. During the ice trials of the RV Sikuliaq, this technique was used to tow fishnets in thin first year ice.

A similar technique is to clear ice behind the vessel while maintaining station in moving sea ice. This is performed by using high power and orienting the wake far enough outboard that the net forward thrust allows the vessel to counteract the ice drift. This technique has been used as a means of actively managing sea ice for offshore facilities [22].

Yet another means of utilizing the propeller wake is to clear an area of around the vessel. A CTD sensor was deployed in a wide variety of ice conditions over the side of the Sikuliaq during its ice trials, by orienting the thrusters such that the ice was broken around that side of the vessel.

Figure 2.1: RV Sikuliaq Clearing Ice for Deployment of CTD.

2.3 Full Scale Data

Although there have been a number of icebreakers designed with azimuth thrusters, there is a limited amount of published data on the ability of propeller wake to break ice. This section summarizes the full scale data that has been previously published, as well as data collected by the author during informal field trials in 2007 (not yet published).

The only published full scale data known to the author are for the MSV Fennica and MSV Botnica [32, 42]. Both vessels were developed in Finland as multipurpose icebreakers, intended for escort operations in the Baltic during the winter and offshore operations during the summer. Fennica is equipped with ducted Aquamaster thrusters, which are configured in the pushing configuration, while Botnica has open Azipod thrusters configured in the pulling orientation. General particulars for both vessels are given in Table 2.1.

Figure 2.2 shows a comparison of the ability of both vessels to break ice using

	Fennica	Botnica
Length O.A.	116 m	96.7 m
Beam MLD.	26.0 m	24.0 m
Draft (Icebreaking)	7.0 m	7.2 m
Propulsion Power	2 x 7.5 MW	2 x 5.0 MW
	Aquamaster	Azipod
	Open Propellers	Ducted Propellers

Table 2.1: General Particulars of MSV Fennica and MSV Botnica [42]

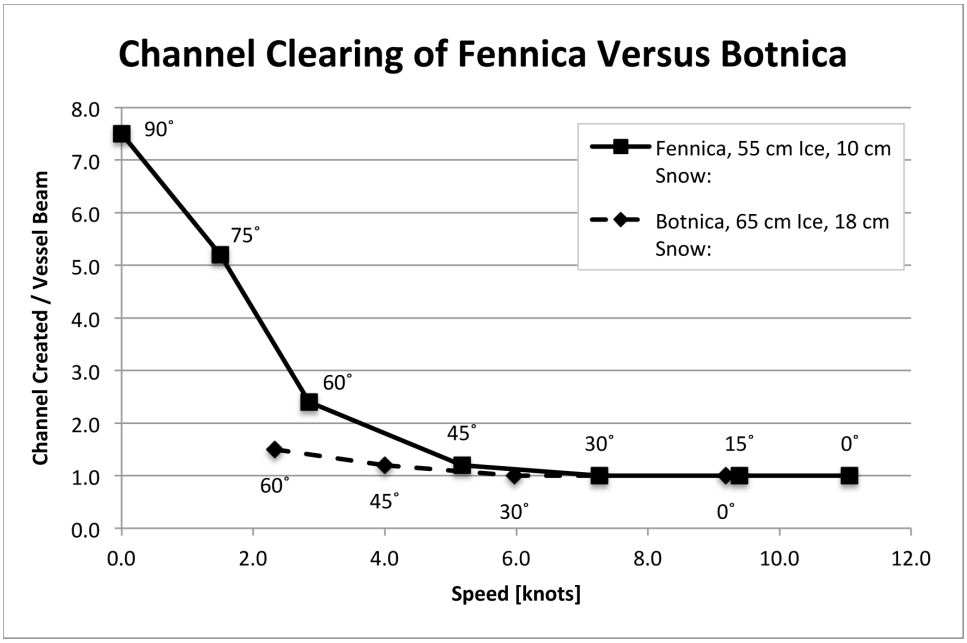

Figure 2.2: Icebreaking Performance with Wake of Fennica and Botnica [42]

the propeller wake. Fennica is capable of breaking ice up to approximately 85 m away from the side of the hull (total width of about 200 m or 7.5 times the ships breadth) in 55 cm of ice with the thrusters orientated outboard. Due to the pulling

configuration and the position of the thrusters, Botnica is unable to use high powers with the thrusters orientated outboard. The differences between these vessels indicate that the variations in thruster design and placement have a considerable impact on the capabilities of the ship.

During the winter of 2007, the author had an opportunity to witness and record the propeller wake breaking ice on both the MSV Fennica and the terminal tug Ahti [33, 34]. Ahti is operated by Neste Oil in Porvoo Finland. General particulars are provided in Table 2.2.

	Ahti
Length O.A.	33.5 m
Beam MLD.	12.8 m
Draft Max.	4.9 m
Main Engine	2 x 2350 kW

Table 2.2: Ahti General Particulars

Both vessels were tested in approximately 30 cm of level ice. During these tests, Ahti was capable of breaking approximately 70 m of ice away from the side of hull at approximately 90% power. The Fennica was able to break ice 170 m away from the side of the hull with full power. With only 25% of the total power, the Fennica was still capable of breaking the ice, with the extent reduced to 90 m from the side of the hull. Although the total power applied by the Fennica was less than Ahti, it was still capable of breaking more ice, in comparable conditions. This indicates that other factors such as the placement, orientation, and size of the propellers likely have

a role to play in the icebreaking capability.

During the trials, the ice appeared to break in a downward manner, with the broken ice pieces being pushed under the ice sheet. This implies that the breaking is a result of reduced hydrodynamic pressure due to accelerated flow under the ice sheet. The wake is also extremely turbulent, as can be observed at the surface. The role of turbulence on the icebreaking is currently unknown.

The importance of orientation was verified during the Ahti trials by heeling the vessel 5°. This resulted in the propellers being oriented such that the wake was directed towards the surface as opposed to being horizontal. Although no noticeable improvements were made to the total amount of ice broken, the time required to break the ice was reduced by a factor of approximately 2.5.

Another factor that made a significant difference in the time required to break the ice was allowing the operator to oscillate the thrusters back and forth around the drive's axis of rotation. This resulted in a more turbulent wake that had the influence of reducing the time required to break the ice.

Both trials performed with the Ahti and Fennica demonstrated that the time required for the ice to break is influenced by the power applied. Lower power settings resulted in a longer delay between the time the power was applied and the time the ice initially broke. It is hypothesized that the delay is a result of the increased time required to accelerate the water under the ice, resulting in longer time to reduce the pressure to the critical point required for the ice to break.

2.4 Design Challenges for Azimuth Icebreakers

Depending on the operational mission of each vessel, the specifics of how azimuth thrusters have been incorporated has varied. Differences between icebreakers equipped with azimuth thrusters have included:

- Propeller design including size, number of blades, pitch, and other propeller geometry
- Propeller operating conditions including power and shaft speed
- Placement on the hull including submergence, mounting angles, and shafting angles
- Nozzled versus open propellers,
- Direct diesel versus electrical driven,
- Z-Drive units versus podded propellers, and
- Pushing versus pulling (tractor) thrusters.

While the work that has been performed previously provides some insight into the operational benefits of existing vessels, there is insufficient knowledge in the physical mechanics to establish the benefits and compromises of the various design choices. Empirical models based on a limited set of full scale data cannot be extrapolated to new vessels with different design configurations with any degree of confidence.

Model scale testing (such as those performed by Ferrieri [13]) provides a partial solution, but are difficult to interpret due to lack of calibration with full scale data.

Without a thorough understanding of the hydrodynamics and ice mechanics involved, scaling relationships cannot be developed to allow interpretation of ice model tests to full scale conditions.

A more thorough understanding of the underlying physical phenomenon is needed to predict how well new azimuth icebreakers will be able to fulfill operational roles. Until such time that this phenomenon can be accurately predicted by industry, it is difficult to justify novel concept designs like the Natural Breaker Drillship proposed by Keinonen [23].

2.5 Background of Panel Method

The original panel method was developed by Hess and Smith for use in the aerospace industry [18]. Since then, it has been widely applied to wing-body problems for aircraft [39, 54, 36, 2, 1]. In the marine sector, the panel method has been applied to a variety of problems including to, but not limited to, seakeeping and propeller design [16, 24, 28, 19, 27, 47, 62, 45, 26].

Greeley and Kerwin applied the panel method to propeller designs to overcome limitations associated with lifting line methods, which were the commonly accepted method of the time [16]. The original method by Greeley and Kerwin was applied to steady state problems. The method relied heavily on model scale experiments to define the specifics of the wake geometry.

Lee further developed the panel method by considering different formulations of the panel method to improve the numerical stability [28]. Lee also applied an iterative Kutta condition to ensure continuity of the pressure at the trailing edge. Hsin applied

panel methods to solve the problem of propellers in unsteady flow [19]. Pyo developed an improved wake alignment scheme by aligning the wake with the three dimensional flow, allowing the concentration of vorticity near the tip to be successfully modelled, and reducing the reliance on model scale data [47]. Recent work has largely focused on developing higher order methods such as the application of B-Splines [26].

The research performed to date has resulted in several variations of the panel method. Some of these codes, such as OpenProp, are available [57]. However, up until recently, these codes have not been designed for computation of the bollard condition, in which the azimuth thrusters are typically used when breaking ice. In addition, as the codes that have been developed are focused on the propeller design, the emphasizes of these codes have been on modelling the near field wake, with the far field wake being considered only to the extent that it influences the near field. A panel method has therefore been developed specifically for this work. The next two chapters provide details related to the specific panel method implemented for the current work.

Chapter 3

Panel Method Theory

The panel method has been selected as a starting point into the investigation for a suitable model to predict the icebreaking with wake phenomenon. Panel methods have been frequently applied to marine propellers and are capable of modelling a wide range of propeller geometry including open and ducted propellers [16, 24, 28, 25, 27, 19, 62]. Panel methods have the additional advantage that they do not require the fluid domain to be divided into a grid. This feature makes them well suited to complex geometries. Panel methods can also be highly efficient as computation is not required in parts of the fluid domain not influenced by the propeller wake.

The panel method is a specific application of the more general boundary element method [6, 3, 7]. Boundary element methods require that the problem be expressed in boundary integral form, which uniquely relates the solution within the domain, to an integral over the domain's surface. The problem is therefore reduced from a 3D problem over the fluid domain to a 2D problem over the fluid boundary. The solution within the fluid domain can then be recovered once the solution on the boundaries is

determined.

The solution to the boundary element method requires identifying a suitable boundary integral form of the problem. The solution on the surface can then be determined by applying suitable boundary conditions. Once the solution on the boundary surface is known, it can then be used to determine the physical parameters of interest within the domain. This chapter is devoted to developing a boundary integral equation for lifting surfaces which can be used for developing a numerical method.

3.1 Problem Statement

3.1.1 Governing Equations for Potential Flow

The boundary element method can only be applied to problems that can be expressed in the boundary integral form. In hydrodynamics, this is possible if the fluid is assumed to be inviscid, incompressible, and irrotational. Under these assumptions, the fluid is said to obey potential flow theory.

Given that the fluid is assumed to follow potential theory, there exists a potential function, Φ, such that the fluid velocity is the gradient of the potential, as given in Equation 3.1. Substituting the potential into the Continuity Equation (Equation 3.2) yields the Laplace Equation (Equation 3.3), which is the governing equation for the panel method.

$$\vec{U}_f = \nabla\Phi \tag{3.1}$$

$$\nabla \cdot \vec{U}_f = 0 \tag{3.2}$$

$$\nabla^2\Phi = 0 \tag{3.3}$$

The boundary element method requires the clear definition of the problem domain in terms of the domain's boundaries. For the lifting bodies, the domain is defined as the fluid around the body as shown in Figure 3.1. For the current work, the problem is defined in a right handed global coordinate system, fixed at the bottom of the ice surface.

The wake surface allows for the exclusion of the vortices that are known to exist behind a lifting body. By excluding this region from the domain, the assumption of irrotational flow is valid even for lifting surfaces.

The fluid is enclosed by the boundary S, which is divided into four parts.

$$S := \{S_B, S_I, S_W, S_\infty\} \tag{3.4}$$

where,

S_B is the body surface,

S_I is the ice surface,

S_W is the surface of the region enclosing the wake,

S_∞ is the far field, represented by a sphere, located at infinity.

3.1.2 Boundary Conditions

To uniquely qualify the problem, boundary conditions are required on all the surfaces of the domain. This section addresses the boundary conditions on each of the four surfaces defined by Equation 3.4.

As the propeller and ice surfaces are rigid bodies, the boundary condition is such that the flux through the bodies' surfaces must be zero (Neumann Boundary Con-

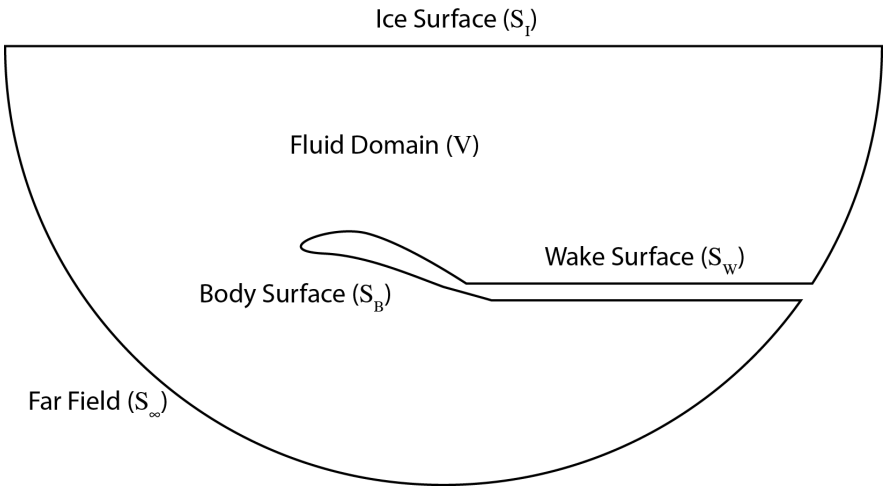

Figure 3.1: Problem Domain

dition). In order for the flux to be zero, the normal component of the fluid velocity must be equal to the normal velocity of the surface. The boundary condition on the rigid surfaces is therefore given as:

$$\hat{n} \cdot \vec{U}_f = \hat{n} \cdot \vec{V}_B \tag{3.5}$$

$$\hat{n} \cdot \nabla\Phi = \hat{n} \cdot \vec{V}_B \tag{3.6}$$

where,

$\vec{U}_f$ - Fluid velocity at the surface

$\hat{n}$ - Unit normal vector

$\vec{V}_B$ - Local velocity of a point on the surface

The propeller is allowed to both translate and rotate. Hence, the velocity of a point on the propeller surface is given by:

$$\vec{V}_B = \vec{V}_G + \vec{\Omega}_B \times \vec{r}_G \tag{3.7}$$

where,

$\vec{V}_G$ - Velocity of the propeller's centre of gravity

$\vec{\Omega}_B$ - Rotational velocity of the propeller

$\vec{r}_G$ - Position vector a point on the propeller relative to the centre of gravity.

Consider the case of a level ice sheet. The bottom of the ice surface can taken to be a horizontal plane that is fixed in space, hence, the vertical component of the velocity should be zero on the ice surface.

$$\hat{k} \cdot \vec{V}_I = \hat{k} \cdot \nabla \Phi_I = 0 \tag{3.8}$$

Far away from the propeller, the flow should not be disturbed. For the sake of generality, the fluid far from the propeller is assumed to be a uniform inflow. The limit of the potential far away from the propeller should therefore be the potential of a steady uniform inflow stream. This is represented by the scalar potential function defined by Equation 3.9. For the specific case of a stationary propeller, the inflow is zero, indicating that the far field potential, Φ_∞, is zero.

$$\lim_{\vec{r} \to \infty} \Phi = \Phi_\infty \tag{3.9}$$

Following the work of Lee [28], the vorticity is assumed to be contained in an infinitely thin volume. Hence, the wake has zero thickness, such that the upper and lower and wake surfaces coincide. For the wake surfaces to represent the vortices shed from the trailing edge, they must be freely convected with the fluid flow. The fluid velocity should therefore be tangential to the wake surface and the pressure difference across the wake surface must be zero.

3.2 Boundary Integral Equation

As required by the boundary element method, the governing equations must be written in the boundary integral form. This is done by applying the divergence theorem to the velocity potential, which converts a three dimensional volume integral into a surface integral as follows:

$$\int_V \nabla \cdot \vec{F} \, dV = -\int_S \hat{n} \cdot \vec{F} \, dS \tag{3.10}$$

In the above equation, $\hat{n}$ is defined as the inward normal vector. Note that the inward normal vector is defined as the vector pointing into the fluid domain (i.e. outwards of the propeller body).

To apply the divergence theorem to the boundary element problem, we first start by letting $\vec{F} = G\nabla\Phi$, where G is a scalar function. The divergence theorem then can be written as:

$$\int_V \nabla\Phi \cdot \nabla G + \Phi\nabla^2 G \, dV = -\int_S \Phi\hat{n} \cdot \nabla G \, dS \tag{3.11}$$

We then define $\vec{F} = \Phi \ \nabla G$. Using this new definition of $\vec{F}$ in the divergence theorem, we obtain the following expression:

$$\int_V \nabla\Phi \cdot \nabla G + G\nabla^2\Phi \, dV = -\int_S G\hat{n} \cdot \nabla\Phi \, dS \tag{3.12}$$

By combining equations 3.11 and 3.12, and recalling from Equation 3.3 that $\nabla^2\Phi = 0$, we can obtain the following expression:

$$\int_V \Phi\nabla^2 G \, dV = \int_S G\hat{n} \cdot \nabla\Phi - \Phi\hat{n} \cdot \nabla G \, dS \tag{3.13}$$

The above equation forms the basis for converting the three dimensional fluid flow problem into a two dimensional boundary element problem.

3.3 Green's Function

Up to this point, the function G has been an arbitrary scalar function. To eliminate the volume integral, and relate the surface integral to the solution within the fluid domain, G is chosen such that:

$$\nabla^2 G = \delta(\vec{r}_{pq}) \tag{3.14}$$

where $\vec{r}_{pq}$ is the vector between points p and q in the fluid domain

$$\vec{r}_{pq} = (x_p - x_q)\hat{i} + (y_p - y_q)\hat{j} + (z_p - z_q)\hat{k}$$

Given the above definition, Equation 3.13 can be rewritten as given below. Hence, the potential anywhere in the fluid domain is related to the solution on the boundaries.

$$\Phi_p = \int_S G\hat{n} \cdot \nabla\Phi - \Phi\hat{n} \cdot \nabla G \; dS \tag{3.15}$$

Furthermore, the function G is chosen as to satisfy the far field boundary conditions. This requires that G be chosen such that the following condition is satisfied:

$$\int_{S_\infty} G\hat{n} \cdot \nabla\Phi - \Phi\hat{n} \cdot \nabla G dS = -\Phi_\infty \tag{3.16}$$

Using this additional constraint, Equation 3.15 can be rewritten to exclude the integral over the far field and the ice surface.

$$\Phi_p = \int_{S_B \cap S_I \cap S_W} G\hat{n} \cdot \nabla\Phi \; dS - \int_{S_B \cap S_I \cap S_W} \Phi\hat{n} \cdot \nabla G \; dS + \Phi_\infty \tag{3.17}$$

To satisfy the above conditions, the function G is given by the three dimensional Green's Function (Equation 3.18).

$$G = -\frac{1}{4\pi|\vec{r}_{pq}|} \tag{3.18}$$

For the case of the level ice sheet, the Green's function can be modified to eliminate the integral over the ice surface, by fulfilling the boundary condition expressed in Equation 3.8. To fulfill the wake boundary condition, the function G is split into two parts. The first part is given by the Green's function, while the second part represents the velocity induced by a virtual panel, which is mirrored across the ice surface. This virtual panel serves to cancel out the vertical velocity components. The numeric form of the function G is given by Equation 3.19.

$$G = -\frac{1}{4\pi}\left(\frac{1}{|\vec{r}_{pq}|} + \frac{1}{|\vec{r}_{pq'}|}\right) \tag{3.19}$$

where,

$$\vec{r}_{pq'} = (x_p - x_q)\hat{i} + (y_p - y_q)\hat{j} + (z_p + z_q)\hat{j}$$

With the above definition of the Green's function, Equation 3.20 can be further simplified to eliminate the influence of the ice sheet. In the case of arbitrary ice surfaces, as is the case with rough ice or icebergs, this simplification cannot be made.

To simplify the notation, only the case of a non-uniform ice sheet is considered and the surface S_B is taken to be the combined body and ice surfaces. Hence, Equation 3.20 is used to represent both scenarios with the choice of G and S_B taken as required depending on the exact context of the problem.

$$\Phi_p = \int_{S_B \cap S_W} G\hat{n} \cdot \nabla\Phi \; dS - \int_{S_B \cap S_W} \Phi\hat{n} \cdot \nabla G \; dS + \Phi_\infty \tag{3.20}$$

3.4 Wake Surface

The wake surface represents the volume of fluid containing the vorticity generated by the propeller. The wake surface therefore consists of both an upper and lower side

such that $S_W := \{S_l \cap S_u\}$, and is bounded by the trailing edge of the propeller and the far field. The vorticity is assumed to be contained in an infinitely thin layer of fluid such that S_l approaches S_u. As $S_l \to S_u$:

$$\lim_{S_l \to S_u} \hat{n}_l = -\hat{n}_u \tag{3.21}$$

$$\lim_{S_l \to S_u} G_l = G_u \tag{3.22}$$

$$\lim_{S_l \to S_u} \nabla\Phi_l = \nabla\Phi_u \tag{3.23}$$

Using the above limits, Equation 3.20 can be evaluated over the wake surface as follows:

$$\begin{aligned}
\int_{S_W} G\hat{n} \cdot \nabla\Phi \; dS &= \int_{S_u} G_u \hat{n}_u \cdot \nabla\Phi_u \; dS + \int_{S_l} G_l \hat{n}_l \cdot \nabla\Phi_l \; dS \\
&= \int_{S_u} G_u \hat{n}_u \cdot \nabla\Phi_u \; dS - \int_{S_u} G_l \hat{n}_u \cdot \nabla\Phi_l \; dS \\
&= \int_{S_u} \hat{n}_u \cdot \left(G_u \nabla\Phi_u - G_l \nabla\Phi_l\right) \; dS \\
&= 0
\end{aligned} \tag{3.24}$$

$$\begin{aligned}
\int_{S_W} \Phi\hat{n} \cdot \nabla G \; dS &= \int_{S_u} \Phi_u \hat{n}_u \cdot \nabla G_u \; dS + \int_{S_l} \Phi_l \hat{n}_l \cdot \nabla G_l \; dS \\
&= \int_{S_u} \Phi_u \hat{n}_u \cdot \nabla G_u \; dS - \int_{S_u} \Phi_l \hat{n}_u \cdot \nabla G_u \; dS \\
&= \int_{S_u} \left(\Phi_u - \Phi_l\right) \hat{n}_u \cdot \nabla G_u \; dS
\end{aligned} \tag{3.25}$$

The potential differential across the wake represents the circulation generate by the propeller blades and is defined by the symbol Γ. Using the above equations, the surface integral in Equation 3.20 can be further simplified.

$$\Phi_p = \int_{S_B} G\hat{n} \cdot \nabla\Phi \; dS - \int_{S_B} \Phi\hat{n} \cdot \nabla G \; dS + \Phi_\infty - \Phi_W \tag{3.26}$$

where,

$$\Phi_W = \int_{S_u} \Gamma \hat{n}_u \cdot \nabla G_u \, dS \tag{3.27}$$

$$\Gamma = \Phi_u - \Phi_l \tag{3.28}$$

3.5 Limit for a Point on the Body Surface

Up to this point, the point P has been assumed to fall within the domain volume V. Due to the definition of the Greens Function, G, Equation 3.26 is singular when the point lies on the body surface ($\vec{r}_p = \vec{r}_q$). In order to provide a useful set of equations, the point P must be allowed to fall on the body's surface, S_B. To remove the singularity, the body's surface is subdivided into two parts defined by $S_B := \{S'_B \cap \Sigma\}$, as shown in Figure 3.2.

- S'_B - The original surface S_B excluding the point P.
- Σ - A hemisphere of radius ϵ centred at P.

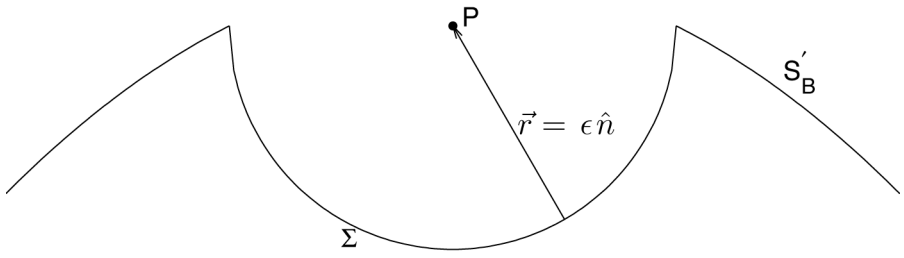

Figure 3.2: Removal of Singularity on the Body Surface.

The limit as ϵ tends to zero is then evaluated to achieve a boundary element equation that can be applied to a point on the bodies surface.

$$\Phi_p = \int_{S'_B \cap \Sigma} G\hat{n} \cdot \nabla\Phi \; dS - \int_{S'_B \cap \Sigma} \Phi\hat{n} \cdot \nabla G \; dS - \Phi_W + \Phi_\infty \tag{3.29}$$

$$\begin{aligned} \int_\Sigma G\hat{n} \cdot \nabla\Phi \; dS &= -\lim_{\epsilon \to 0} \int_\Sigma \frac{\hat{n} \cdot \nabla\Phi}{4\pi r} \; dS \\ &= -\lim_{\epsilon \to 0} \frac{2\pi\epsilon^2}{4\pi\epsilon} \hat{n} \cdot \nabla\Phi \\ &= 0 \end{aligned} \tag{3.30}$$

$$\begin{aligned} \int_\Sigma \Phi\hat{n} \cdot \nabla G \; dS &= -\lim_{\epsilon \to 0} \int_\Sigma \frac{\Phi}{4\pi} \hat{n} \nabla \frac{1}{r} \; dS \\ &= -\lim_{\epsilon \to 0} \int_\Sigma \frac{\Phi}{4\pi r} \frac{\hat{n} \cdot \vec{r}}{r^3} \; dS \\ &= -\lim_{\epsilon \to 0} \int_\Sigma \frac{\Phi}{4\pi r^2} \; dS \\ &= -\Phi_p \lim_{\epsilon \to 0} \frac{2\pi\epsilon^2}{4\pi\epsilon^2} \\ &= -\frac{1}{2}\Phi_p \end{aligned} \tag{3.31}$$

Using the above results, Equation 3.26 can be expressed as the integral over the surface S'_B, which represents the surface S_B with an infinitesimal point around P excluded from the surface.

$$\int_{S'_B} G\hat{n} \cdot \nabla\Phi \; dS - \int_{S'_B} \Phi\hat{n} \cdot \nabla G \; dS - \int_{S_u} \Gamma\hat{n}_u \cdot \nabla G_u \; dS + \Phi_\infty = \begin{cases} \Phi_p & p \in V \\ \frac{1}{2}\Phi_p & p \in S \\ 0 & p \notin V \cap p \notin S \end{cases} \tag{3.32}$$

3.6 Internal Potential

The above equation could be used directly to develop the panel method. However, to further simplify the problem, we continue following the work of Lee by introducing a fictious potential flow inside the body, Φ_i [28]. Equation 3.15 is then applied to the internal potential following the methodology outlined above. However, as the potential is defined internal to the body (external to the fluid), we obtain Equation 3.33. Hence, the presence of the internal potential does not influence the solution to the original problem.

$$0 = \int_{S'_B} G\hat{n} \cdot \nabla\Phi_i \, dS - \int_{S'_B} \Phi_i \hat{n} \cdot \nabla G \, dS \tag{3.33}$$

Subtracting 3.33 from 3.32 gives (for $P \in S$):

$$\frac{1}{2}\Phi_p = \int_{S'_B} G\hat{n} \cdot \nabla \left(\Phi - \Phi_i\right) \, dS - \int_{S'_B} \left(\Phi - \Phi_i\right) \hat{n} \cdot \nabla G \, dS - \Phi_W + \Phi_\infty \tag{3.34}$$

The dipole and source strengths are then defined as:

$$\mu = \Phi - \Phi_i \tag{3.35}$$

$$\sigma = \hat{n} \cdot \nabla(\Phi - \Phi_i) = \hat{n} \cdot \left(\vec{V}_B - \nabla\Phi_i\right) \tag{3.36}$$

Using the above definitions, the boundary integral equation can be written as:

$$\int_{S'_B} G\sigma \, dS - \int_{S'_B} \mu\hat{n} \cdot \nabla G \, dS - \int_{S_u} \Gamma\hat{n}_u \cdot \nabla G_u \, dS + \Phi_\infty = \begin{cases} \Phi_p & p \in V \\ \frac{1}{2}\Phi_p & p \in S \\ 0 & p \notin V \cap p \notin S \end{cases} \tag{3.37}$$

As the internal potential, Φ_i, does not influence the solution of the problem, the choice of internal potential is arbitrary. However, the choice of internal potential influences the resulting numerical approach. Lee developed and compared a variety of panel methods depending on the choice of internal potentials [28]. For the panel method developed in Chapter 4, the internal potential is set to zero, $\Phi_i = 0$, such that the dipole strength is the fluid velocity potential and the source strength is the fluid velocity normal to the body.

3.7 Body Pressures

Before Equation 3.37 can be solved for the fluid potentials on the body surface, the circulation, Γ, must be related to the surface potentials, Φ. This is done through the wake surface boundary conditions. In order to ensure that the pressure is continuous across the wake, the Kutta condition must be satisfied, which requires that the pressure be continuous across the trailing edge. It is therefore necessary to be able to compute the pressures on the surface of the body. The pressure on the body surface is determined following the work of Willis [59]. Further details on the pressure in potential flow can be found in the works of Segletes and Walters [53].

The pressures are determined based on Bernoulli's equation for unsteady, irrotational flow.

$$-\frac{\nabla P}{\rho} = \frac{\partial \vec{U}_f}{\partial t} + \vec{U}_f \cdot \nabla \vec{U}_f \tag{3.38}$$

In regions with zero vorticity, this is equivalent to Equation 3.39.

$$-\frac{\nabla P}{\rho} = \frac{\partial \vec{U}_f}{\partial t} + \frac{1}{2}\nabla \left|\vec{U}_f\right|^2 \tag{3.39}$$

Using the definition of the velocity given in Equation 3.1, the above can be expressed in terms the fluid potential:

$$\frac{\nabla P}{\rho} + \nabla \frac{\partial \Phi}{\partial t} + \frac{1}{2} \nabla \left| \nabla \Phi \right|^2 = 0 \tag{3.40}$$

The above expression can be integrated along a streamline from a point in the far field to a point on the body. This produces the familiar version of the Bernoulli equation for unsteady, irrotational flow.

$$\frac{P - P_\infty}{\rho} + \frac{\partial \Phi}{\partial t} + \frac{1}{2} \left| \nabla \Phi \right|^2 = 0 \tag{3.41}$$

The above equation is given in a Eulerian reference frame. As the point of interest is on a body in motion, the time derivatives must be converted to a Lagrangian reference frame using the material derivative. The Eulerian time derivative can therefore be substituted with the convective time derivative.

$$\frac{D\Phi}{Dt} = \frac{\partial \Phi}{\partial t} + \vec{V}_B \cdot \nabla \Phi \tag{3.42}$$

$$\frac{P - P_\infty}{\rho} + \left(\frac{D\Phi}{Dt} - \vec{V}_B \cdot \nabla \Phi \right) + \frac{1}{2} \left| \nabla \Phi \right|^2 = 0 \tag{3.43}$$

The pressure at a point in the far field, P_∞, can be evaluated using Equation 3.43. Substituting the result back into Equation 3.43 yields the final form of the Bernoulli equation:

$$P = \rho \left[\vec{V}_B \cdot \vec{U}_f - \frac{1}{2} \left| \vec{U}_f \right|^2 + \frac{1}{2} \left| \vec{U}_\infty \right|^2 - \frac{D\Phi}{Dt} \right] \tag{3.44}$$

In the current work, the propeller is assumed to be operating at a steady state. As such, the problem is steady in a Lagrangian sense, such that the potential on any given panel does not change with time. Hence, the time derivative in Equation 3.44 is taken as zero. The non-steady case can be recovered by including the time rate of change of the solution.

3.8 Summary

This chapter has presented the fundamental theory required to develop a panel method for lifting surfaces. The solution to the problem consists of solving the boundary element integral given by Equation 3.37 for the unknown dipole strengths, μ, on the body surface. Once the dipole strengths, and hence the body potentials, are known the velocities in the fluid domain, and hence near the ice surface, can be computed by taking the gradient of the boundary element integral. Once the fluid velocities have been determined, the Bernoulli equation (Equation 3.44) can be used to determine the fluid pressures.

The wake circulation must be chosen to satisfy the Kutta condition, which requires that the pressure differential across the wake is zero. The wake must also be aligned with the fluid flow as required by the boundary conditions.

As there are no general closed form solutions for these equations, a numerical approach is required. The numerical approach used for this work is described in the next chapter.

Chapter 4

Panel Method Implementation

In order to solve the boundary integral equation developed in Chapter 3, a numerical approach is required. A panel method code applicable to lifting surfaces has been implemented to solve the numerical problem. This chapter describes the approach used in the code developed for this work.

The premise of the numerical approach is to divide the body and wake surfaces into discrete panels, each representing a portion of the surface. The surface integrals are then replaced by a summation of integrals computed over each surface panel, as discussed in Section 4.1. The integral over each surface can be solved analytically by assuming a simplified geometry and potential distribution for each panel, as discussed in Section 4.2. This allows the integral equation to be replaced with a matrix equation, which can be solved using a variety of computational techniques.

Once the surface potentials are known, the velocities both on the surfaces as well as within the fluid domain are required. Velocities in the fluid domain can be determined analytically by taking the gradient of the boundary integral equation. However, the

velocity on the surfaces requires special consideration. This is discussed further in Section 4.3.

Complications arise due to the unknown circulation, Γ, and the geometry of the wake. The unknown circulation must be related to surface potentials using the Kutta condition. This is discussed further in Section 4.4. The Kutta condition ensures that there is no pressure jump across the wake as required by the boundary conditions. This generates an additional set of equations, which must be solved simultaneously with the boundary element equations.

The location of the wake surfaces is not known a priori, as it must be aligned with the unknown fluid flow. Rather, the geometry of the wake surfaces must be solved iteratively as part of the computational scheme. The typical approach is to first solve the problem using a pre-specified geometry. The wake geometry is then aligned with the flow and a new solution is determined. This is repeated until the wake is suitably aligned to the flow. This is discussed further in Section 4.5.

4.1 Discretization of Boundary Element Integral

The numerical solution to the boundary element problem consists of solving Equation 3.37 for the unknown dipole strengths, μ, and wake circulations, Γ. To discretize the boundary element integral the propeller surface is divided into N_b discrete surface panels.

The wake surface is divided into N_w strips of panels, one for each edge of the body defined to be wake shedding. Each strip consists of N_v panels such that the wake geometry can be approximated by discrete panels. Each panel in a given strip

is associated a circulation value, which is constant along the length of the wake strip.

The integrals are then replaced with the summation of integrals over each surface panel. In the current method, the potential has been taken as constant over each panel. This allows the potential, as well as the normal velocity term, to be taken outside of the integrals as expressed below.

$$\begin{aligned}
\frac{1}{2}\Phi_p &= \sum_q^{N_b} \int_{S_q} G\sigma_q \, dS - \sum_{q\neq p}^{N_b} \int_{S_q} \mu_q \vec{n}_q \cdot \nabla G \, dS \\
&\quad - \sum_w^{N_w} \sum_v^{N_v} \int_{S_w} \Gamma_w \vec{n}_v \cdot \nabla G \, dS + \phi_\infty \qquad (4.1) \\
&= \sum_q^{N_b} \sigma_q \int_{S_q} G \, dS - \sum_{q\neq p}^{N_b} \mu_q \int_{S_q} \vec{n}_q \cdot \nabla G \, dS \\
&\quad - \sum_w^{N_w} \Gamma_w \sum_v^{N_v} \int_{S_v} \vec{n}_v \cdot \nabla G \, dS + \phi_\infty \qquad (4.2) \\
&= \sum_q^{N_b} \sigma_q G_{pq} - \sum_{q\neq p}^{N_b} \mu_q H'_{pq} - \sum_w^{N_w} \Gamma_w W_{pw} + \phi_\infty \qquad (4.3)
\end{aligned}$$

$$\begin{aligned}
G_{pq} &= \int_{S_q} G \, dS \qquad (4.4) \\
H'_{pq} &= \int_{S_q} \vec{n}_q \cdot \nabla G \, dS \qquad (4.5) \\
W_{pw} &= \sum_v^{N_v} \int_{S_v} \vec{n}_v \cdot \nabla G \, dS \qquad (4.6)
\end{aligned}$$

The coefficients G_{pq} and H'_{pq} represent the influence of a panel at point q on a panel at point p, while W_{pw} represents the influence of the w^{th} wake strip on the panel p. These coefficients are therefore referred to as influence coefficients.

Noting that $\mu_p = \Phi_p$ lies both on the left hand side of Equation 4.3 and within the summation on the right hand side, Equation 4.3 can be further simplified by moving

Φ_p within the summation.

$$\sum_{q}^{N_b} \sigma_q G_{pq} = \sum_{q}^{N_b} \mu_q H_{pq} + \sum_{w}^{N_w} \Gamma_w W_{pw} + \phi_\infty \tag{4.7}$$

$$H_{pq} = \begin{cases} H'_{pq} & p \neq q \\ \frac{1}{2} & p = q \end{cases} \tag{4.8}$$

These equations can be written in matrix form as:

$$\bar{G}\tilde{\sigma} = \bar{H}\tilde{\mu} + \bar{W}_o\tilde{\Gamma} + \tilde{\phi}_\infty \tag{4.9}$$

The above equations are to be solved for the unknown vector quantities $\tilde{\mu}$ and $\tilde{\Gamma}$. The matrices $\bar{G}$ and $\bar{H}$ depend only on the geometry of the body surface and will be discussed in Section 4.2. The vector $\tilde{\sigma}$ depends only on the boundary conditions as given by Equation 3.36. The matrix $\tilde{W}_o$ depends on the location of the wake, which will be discussed in Section 4.5.

4.2 Body Discretization

4.2.1 Geometry

The body geometry is to be discretized into individual panels. To simply the integrals in Equations 4.4 to 4.6, the panels have been taken as planar surfaces, referred to as Flat Panels, as shown in Figure 4.1. More complex geometries have been considered by others that account for curvature in the panels [19, 26]. Flat panels have been chosen for this work due to their simplicity.

The panel discretization used for this work follows similar conventions as those used in VSAERO [36]. Panels consist of either three or four coplanar nodes. For the

purpose of the discussion below, a panel is assumed to consist of four nodes. This does not result in any loss of generality as panels with three nodes can be easily obtained by using the same coordinates for two consecutive nodes. When creating four sided panels from points that lie on the body, the coordinates are not generally coplanar. The actual panel nodes must therefore be determined by projecting the body coordinates onto a plane.

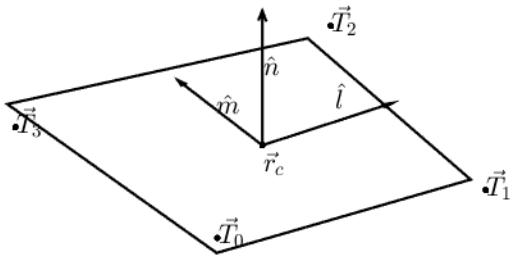

Figure 4.1: Geometry of a Flat Panel.

The plane of the panel is defined based on its normal vector, $\hat{n}$ and the panel's centroid, $\vec{r}_c$. The centroid is calculated as the average of all non-duplicated nodes supplied by the user, $\vec{T}_i$ where $i \in \{0, 1, 2, 3\}$, according to Equation 4.10. The normal vector to the panel is calculated as the cross product of the diagonal vectors. The direction of the normal vector is based on the order of the nodes. To be consistent with the theory developed in Chapter 3, the order of the nodes must be taken in a counter-clockwise order such that when applying the right hand rule, the normal

points out of the body (i.e. into the fluid). The magnitude of the normal vector is also used to calculate the area of the panel, which will be required when evaluating the surface integrals in Section 4.2.2.

$$\vec{r}_c = \frac{1}{N_n} \sum \vec{T}_i \tag{4.10}$$

$$\hat{n} = \frac{\vec{d}_1 \times \vec{d}_2}{\left|\vec{d}_1 \times \vec{d}_2\right|} \tag{4.11}$$

$$A = \frac{1}{2} \left|\vec{d}_1 \times \vec{d}_2\right| \tag{4.12}$$

$$\vec{d}_1 = \vec{T}_2 - \vec{T}_0 \tag{4.13}$$

$$\vec{d}_2 = \vec{T}_3 - \vec{T}_1 \tag{4.14}$$

The panel nodes are determined as the projection of the user supplied coordinates on the plane given by $\hat{n}$ and R_c. The projection is performed by defining two in plane coordinate vectors, $\hat{l}$ and $\hat{m}$. $\hat{m}$ is defined as the vector extending from the centroid to the midpoint between nodes 2 and 3. $\hat{l}$ is then defined to be perpendicular to both $\hat{m}$ and $\hat{n}$.

$$\vec{r}_i = \left\langle \left(\vec{T}_i - \vec{r}_c\right) \cdot \hat{l}, \left(\vec{T}_i - \vec{r}_c\right) \cdot \hat{m}, 0 \right\rangle \tag{4.15}$$

$$\hat{m} = \frac{\frac{1}{2}\left(\vec{T}_2 + \vec{T}_3\right) - \vec{r}_c}{\left|\frac{1}{2}\left(\vec{T}_2 + \vec{T}_3\right) - \vec{r}_c\right|} \tag{4.16}$$

$$\hat{l} = \hat{m} \times \hat{n} \tag{4.17}$$

4.2.2 Evaluation of the Boundary Element Integrals

4.2.2.1 Exact Formulation

The solution to the boundary element integrals in Equations 4.4, 4.5, and 4.6 are required in addition to their gradients. The formulations used have been adapted from Hess [18], Morino [39], and Maskew [36].

The influence of G is evaluated by considering the influence of the panel to be the superposition of the influence from each side. Based on this formulation, the influence coefficients are calculated for each side and summed. The calculation is performed in the panels' local coordinate system, $\langle \xi, \eta, \zeta \rangle$, centred at the panel's centroid.

$$\begin{aligned}
4\pi G_{pq} &= \int_{S_q} G \; dS \\
&= \sum_{i=1}^{n} \left[R_{ij} Q_{ij} - \zeta_p J_{ij} \right] && (4.18) \\
4\pi \nabla G_{pq} &= \int_{S_q} \nabla G \; dS \\
&= \sum_{i=1}^{n} Q_{ij} \frac{(\eta_j - \eta_i)}{d_{ij}} \hat{\xi} - Q_{ij} \frac{(\xi_j - \xi_i)}{d_{ij}} \hat{\eta} + J_{ij} \hat{\zeta} && (4.19) \\
4\pi H_{pq} &= \hat{n}_q \cdot \nabla G_{pq} = J_{ij} && (4.20) \\
4\pi \nabla H_{pq} &= \frac{\left(|\vec{r}_i| + |\vec{r}_j| \right) \vec{r}_i \times \vec{r}_j}{|\vec{r}_i||\vec{r}_j| \left(|\vec{r}_i||\vec{r}_j| + \vec{r}_i \vec{r}_j \right)} && (4.21)
\end{aligned}$$

$$R_{ij} = \frac{(\eta_j - \eta_i)(\xi_p - \xi_i) - (\xi_j - \xi_i)(\eta_p - \eta_i)}{d_{ij}} \tag{4.22}$$

$$Q_{ij} = \log\left[\frac{|\vec{r}_i| + |\vec{r}_j| + d_{ij}}{|\vec{r}_i| + |\vec{r}_j| - d_{ij}}\right] \tag{4.23}$$

$$\tan(J_{ij}) = \frac{R_{ij}\,|\zeta_p|\,(|\vec{r}_j| s_j - |\vec{r}_i| s_i)}{|\vec{r}_i||\vec{r}_j| R_{ij}^2 + s_i s_j \zeta_p^2} \tag{4.24}$$

$$|\vec{r}_i| = \sqrt{(x - \xi_i)^2 + (y - \eta_i)^2 + z^2} \tag{4.25}$$

$$d_{ij} = \sqrt{(\xi_j - \xi_i)^2 + (\eta_j - \eta_i)^2} \tag{4.26}$$

$$s_i = \frac{(\xi_i - \xi_p)(\xi_j - \xi_i)}{d_{ij}} + \frac{(\eta_i - \eta_p)(\eta_j - \eta_i)}{d_{ij}} \tag{4.27}$$

$$s_j = \frac{(\xi_j - \xi_p)(\xi_j - \xi_i)}{d_{ij}} + \frac{(\eta_j - \eta_p)(\eta_j - \eta_i)}{d_{ij}} \tag{4.28}$$

where,

$\langle \xi_p, \eta_p, \zeta_p \rangle$ - Coordinate of the field point, p

$\langle \xi_i, \eta_i \rangle$ - Coordinate of the panel node, i

n - Number of nodes on the panel

$\vec{r}_i$ - The vector from node i, to the field point, p

j - The panel node next to node i, $j = (i+1) \mod n$

In the specific case of the level ice sheet, the influence coefficients are first computed by considering only the component of $G_O = -\frac{1}{4\pi|\vec{r}_{pq}|}$. The contribution of G_H is determined by computing the influence of panel q on point p' (p mirrored across the xy plane), and then reflecting the solution back across the plane.

4.2.2.2 Multipole Expansion

The computation of the influence coefficients is computationally expensive, and must be computed for a large number of field points. Hence, an approximate solution that

is more computationally efficient is desirable to speed up the calculations. This can be achieved by noting that far away from the panel the exact geometry has little effect on the influence coefficients.

Provided the field point is located far away from the panel, the position vector, $\vec{r}_{pq}$, can be approximated as a constant over the surface of the panel. With this approximation, the above integrals can be simplified. The approximated solutions to Equations 4.18 to 4.21 are given in Equations 4.29 to 4.32.

$$G_{pq} \approx \frac{-A_q}{4\pi|\vec{r}_{pq}|} \tag{4.29}$$

$$\nabla G_{pq} \approx \frac{A_q}{4\pi|\vec{r}_{pq}|^3}\vec{r}_{pq} \tag{4.30}$$

$$H_{pq} \approx \frac{A_q}{4\pi|\vec{r_{pq}}|^3}\left(\hat{n}\cdot\vec{r}_{pq}\right) \tag{4.31}$$

$$\nabla H_{pq} \approx -\frac{A_q}{4\pi|\vec{r}_{pq}|^5}\left(3\left(\hat{n}\cdot\vec{r}_{pq}\right)\vec{r}_{pq} - |\vec{r}_{pq}|^2\hat{n}\right) \tag{4.32}$$

where, A_q is the area of the panel q.

This simplified solution can be used without introducing significant errors when the field point is sufficiently far away from the panel. In the current implementation, the cutoff distance can be entered as a multiple of the panel size. The size of the panel is the average of the distance between the centroid and the midpoint of the four edges.

The influence of the multipole assumption on the accuracy of the source and dipole influence coefficients is shown in Figure 4.2. The absolute error in the coefficients has been plotted as a function of the distance between the panel centroid and the field point, normalized by the panel size. The results are for a square panel and a field point located along the panel's normal vector. The results show that for a cutoff distance of 10 times the size of the panel, the absolute error is less than 10^{-4}. This

cutoff value has been used in all calculations performed in this work.

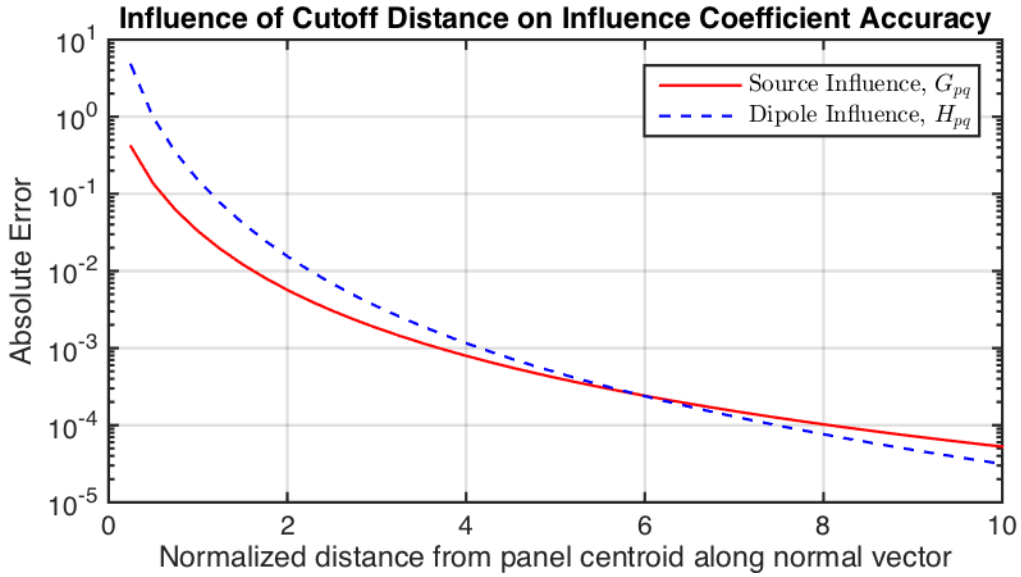

Figure 4.2: Accuracy of Multiple Expansion Formulation

4.3 Fluid Velocities

4.3.1 Off Body Fluid Velocity

The fluid velocity for points off the body can be computed directly by taking the gradient of Equation 3.32. Following Section 4.1, the body surface integrals are discretized and replaced with integrals over the flat panels with constant potentials. This produces a matrix equation for the fluid velocities based on the known potentials and circulations. The gradients of the influence matrices have already been presented

in Section 4.2.2.

$$\begin{aligned}\vec{U}_f = \nabla\Phi &= \int_{S'_B} \sigma \nabla G \; dS - \int_{S'_B} \mu \nabla \left(\hat{n} \cdot \nabla G\right) \; dS \\ &\quad - \int_{S_W} \Gamma \nabla \left(\hat{n} \cdot \nabla G_u\right) \; dS + U_\infty \qquad (4.33)\\ \nabla\Phi &= \sum_p^{N_p} \sigma_p \nabla G_{pq} - \sum_p^{N_p} \mu_p \nabla H_{pq} - \sum_k^{N_k} \Gamma_k W_{kp} + U_\infty \qquad (4.34)\end{aligned}$$

4.3.2 On Body Velocity Field

Due to the singularities on the surface, the above formulation cannot be used to evaluate the velocities at the surface. Therefore, the velocity field on the body's surface is determined through numerical differentiation of the potential values. The method adopted is a variant of that used by Maskew [36].

Once the potentials on the surface are known the surface gradients in the directions of the panels, $\vec{t_p^i}$, can be computed using Equation 4.35. For a four sided panel connected to adjacent panels on all four sides, Equation 4.35 represents four equations. An additional equation can be obtained by considering the no-flux boundary condition given by Equation 3.6. In total, this yields five equations for the three unknown velocity components, U_x, U_y, and U_z. As the system is over determined, the velocity is determined using the method of least squares.

$$\frac{\vec{t_p^i}}{|\vec{t_p^i}|} \cdot \vec{U} = \frac{\Phi_q - \Phi_p}{|\vec{t_p^i}| + |\vec{t_q^j}|} \qquad (4.35)$$

where,

Φ_p - The potential of panel p.

Φ_q - The potential of the neighbouring panel p.

i - The edge of panel p adjacent to panel q.

j - The edge of panel q adjacent to panel p.

$\vec{t}_p^{\,i}$ - The vector from the centroid of panel p to the midpoint of the edge i

$\vec{t}_q^{\,j}$ - The vector from the centroid of panel q to the midpoint of the edge j

Only two non-collinear neighbours must be considered to determine the fluid velocity, hence, the above approach is still valid for triangular panels. Special consideration is also given to panels at the trailing edge, so that the numerical gradient is not computed across the sharp corner at the trailing edge.

4.4 Kutta Condition

4.4.1 Pressure Kutta Condition

The boundary element integral in Equation 4.9 requires the solution of N_b potentials (one for each panel) and N_w circulations. As the matrix equations only represent N_b equations, the solution is under-determined and additional constraints are required to obtain a unique solution. The additional constraints are determined by considering the pressure at the trailing edge of the propeller as proposed by Lee [28]. Lee proposed that the difference in pressure between the upper and lower panels forming the trailing edge should be equal in order to fulfill the Kutta condition.

Lee [28] proposed a pressure kutta condition that iteratively solves for the unknown circulations, Γ, required to eliminate the pressure difference across the trailing edge. The solution consists of solving for Equation 4.36, where the function f represents the boundary value problem represented by Equation 4.9 and the Bernoulli

equation from Section 3.7.

$$\Delta P_{te} = f(\Gamma) \tag{4.36}$$

The problem is solved using a multidimensional root finding algorithm based on the Newton-Raphson method [46]. The iterative solution requires that the boundary element problem be solved with an assumed value for the circulation. The pressure difference is then computed across each segment of the trailing edge. The solution is then recomputed using small changes in the circulation for each segment in order to determine the Jacobian. A new estimate of the circulation is then determined using the Newton-Raphson method. This process is then repeated until the pressure difference is within an acceptable tolerance.

4.4.2 Morino Kutta Condition

Although the method above provides an accurate representation of the Kutta condition, it requires an initial estimate. Therefore, an approximate solution is desired to use as a starting point to the iterative algorithm. A Kutta condition was proposed by Morino [38] based upon the definition of the circulation as the potential difference across the wake, as given in Equation 3.28. By relating the potential difference across the wake to the potential of the panels adjacent to the leading edge, Equation 4.9 can be written to eliminate the circulation from the right hand side of the equations, as given in the equations below. The wake influence matrix, $\bar{W}$, represents the matrix $\bar{W}_o$ rearranged such that the influence terms are applied to the potentials corresponding to the upper and lower panels connected to the trailing edge.

$$\Gamma = \Phi_u - \Phi_l = \mu_u - \mu_l \tag{4.37}$$

$$\bar{W}_o \tilde{\Gamma} = \bar{W} \tilde{\mu} \tag{4.38}$$

$$\bar{G} \tilde{\sigma} = \left(\bar{H} + \bar{W} \right) \tilde{\mu} + \tilde{\phi}_\infty \tag{4.39}$$

It should be noted that the solution to Equation 4.37 only represents the exact solution in the case of two dimensional flows. For bodies with significant cross flows, such as is the case for low aspect ratio airfoils such as propellers, Equation 4.39 leads to significant differences in pressure at the tip of the lifting surface [28].

Equation 4.39 is therefore used to provide an initial estimate of the circulation, ignoring any three dimensional influences. By eliminating the circulation, Equation 4.39 can be solved for the dipole strengths, μ, which in turn can be used to generate the first estimate of the circulation, Γ, using Equation 4.37. This initial estimate for the circulation is then refined based on the iterative method discussed in Section 4.4.1.

4.5 Wake Geometry

In order for there to be no velocity component normal to the wake panels, the position of the wake must be aligned with the local velocity. This problem has been addressed by other researchers [16, 24, 28, 47, 14]. The model developed by Greeley et al. [16, 24, 28] consists of defining the radial position of the wake vortices from data obtained from model scale experiments. These vortices are then wrapped around a cylinder at a specified pitch angle to generate the wake panels. The wake far from the propeller is approximated using various alternative analytical schemes instead of

being modelled by wake panels [16, 28]. The wake alignment scheme used consists of varying the pitch of the wake based on the induced velocities. This does not provide an exact solution as the radial velocity components are not accounted for in the alignment scheme.

Pyo [47] developed an approach for arbitrarily aligning the wake in three dimension, which has been successfully used by others [14, 45, 48, 55]. Pyo's model consisted of evaluating the velocity at each wake panel and adjusting the position of the wake according to the local velocity field.

This approach was attempted for the current work, using flat, constant strength panels. Due to the fact that the velocities are ill-defined on the corners of the panels, and that flat panels are not suitable for modelling the highly curved surface near the tips, such a method was not feasible using the current approach. To accurately model wake roll-up a rigorous numerical scheme is required.

Pyo's method was capable of overcoming these challenges by utilizing hyperboloid panels, as well as bi-quadratic strength panels to achieve the level of a numerical stability required to achieve wake roll-up. However, the complexity of modelling the wake is expected to increase the further downstream from the propeller the problem is being computed. The assumption of an infinitely thin wake sheet far downstream is also expected to influence the accuracy of this approach. Pyo's work focused on modelling the performance of the propeller, and was therefore only concerned with the wake close to the propeller.

In addition, the alignment of wake panels is expected to be poorly suited to modelling the interaction of the wake with objects downstream of the propeller as the panelized wake must be deformed such that it does not penetrate the ice.

Due to the challenges of aligning a panelized wake with the complex flow downstream of the propeller interacting with an object, this approach was deemed to be unsuited to the current application. Hence, the panel method as presented in this chapter has been disqualified as a suitable method of predicting the ice breaking and clearing phenomenon.

The next section discusses an alternative wake representation that has been explored to overcome the limitation of the panel method.

Chapter 5

Vortex Particle Method

Vortex particle methods have been identified as an alternative method of overcoming the challenges encountered with the three dimensional wake alignment scheme in the panel method. Cottet [11] provides a thorough analysis of the field of vortex particle methods, while Winckelmans [61] provides an excellent overview.

The vortex particle method has been a relatively new approach utilized by the aeronautics industry. The vortex particle methods have been applied to helicopter rotors by Opoku et al. followed by He et al. [43, 17]. Willis used the vortex particle method for the computation of wakes of fixed wing aircraft [59]. The most recent application has been by Calabretta, who approximated an aircraft propeller by an actuator disc to compute the influence of the propeller wake flowing over the downstream wing [8]. There is no known attempt to apply vortex particle methods to a marine propeller. In each of the cases above, vortex particle methods have been applied in combination with a panel method. This approach will be followed here.

The vortex particle method is capable of modelling the vorticity of the fluid di-

rectly instead of using dipole panels as was the case in the panel method. This requires a different set of governing equations than was presented in Chapter 3. The governing equations, followed by the boundary conditions as they apply to the vortex particle method, are presented in Section 5.1. This section ends with a discussion of the application of the Bernoulli equation in the vortex particle method.

Analogous to the panel method, in order to develop a numerical method, the vorticity must be discretized into elements. Using the vortex particle method, the vorticity in the wake is represented by a cloud of particles. Each particle contributes to the overall fluid velocity in proportion to its associated circulation. The discretization of vorticity into vortex particles is the foundation of the vortex particle method, which is presented in Section 5.2.

In the vortex particle method the wake alignment is performed by modelling the evolution of individual vortices. As the vortices are convected downstream with the fluid flow, wake alignment is automatically achieved. The shedding of vortex particles from the trailing edge and their subsequent evolution downstream is discussed in Section 5.3. As strict connectivity between particles within the wake is not required, the numerical complexity of maintaining a well behaved wake sheet (as is required in the panel method) is eliminated.

5.1 Theory

5.1.1 Governing Equations

As vortex particles model the vorticity within the fluid domain, the assumption of irrotational flow required for the panel method can be lifted. The definition of fluid velocity as a potential gradient (Equation 5.1) is therefore no longer applicable. Following the work of Willis [56, 59], the velocity field is divided into an irrotational (curl-free) vector field and a rotational (divergence-free) vector field using Helmholtz decomposition (Equation 5.1). The irrotational velocity field is represented by the scalar potential function, Φ, while the rotational component of the flow is represented by the vector potential function, $\vec{\Psi}$.

$$\begin{aligned} \vec{U} &= \vec{U}_{\Phi} + \vec{U}_{\Psi} \\ &= \nabla\Phi + \nabla \times \vec{\Psi} \end{aligned} \tag{5.1}$$

As will be shown in this chapter, the decomposition of the problem into irrotational and rotational velocity components allows the problem to be solved by a superposition of the panel method and vortex particle method. The vector velocity potential is used to represent the vorticity in the wake, while the scalar potential represents the influence of the rigid surfaces.

The vorticity is defined as the curl of the velocity field. Applying this definition to the velocity defined in Equation 5.1, yields a relationship between the vorticity and the vector potential. Due to the vector velocity field being divergence free ($\nabla \cdot \vec{\Psi} = 0$), the curl of the velocity field is given as the negative of the Laplacian of the vector potential. The irrotational potential field does not contribute the total vorticity,

which is consistent with the requirement for potential flow to be irrotational.

$$\vec{\omega} = \nabla \times \vec{U} = -\nabla^2 \vec{\Psi} \tag{5.2}$$

The governing equations for an inviscid, incompressible fluid are the Euler equations, given by Equation 5.3. To obtain a form which is useful for vortex particle methods, the curl of the Euler equations is taken in order to obtain the vorticity evolution equation given by Equation 5.4. The vorticity equations define how the vorticity changes with time as a result of gradients in the velocity field. This equation will form the basis for the wake evolution in Section 5.3.2.

$$\frac{\partial \vec{U}}{\partial t} + \vec{U} \cdot \nabla \vec{U} = -\frac{\nabla P}{\rho} \tag{5.3}$$

$$\frac{D\omega}{Dt} = \frac{\partial \omega}{\partial t} + \vec{U} \cdot \nabla \vec{\omega} = \vec{\omega} \cdot \nabla \vec{U} \tag{5.4}$$

To determine the solution for the scalar potential, the Helmholtz decomposition definition of the velocity (Equation 5.1) is substituted into the Continuity equation (Equation 3.2). As the divergence of the rotational velocity component is zero, the result is the Laplace Equation for the scalar potential (Equation 3.3).

$$\nabla \cdot \vec{U} = \nabla^2 \Phi = 0 \tag{5.5}$$

As the scalar potential is governed by the same boundary element integral as used in the panel method, it can be solved using the panel method developed in Chapter 4. However, due to the influence of the vorticity, the boundary conditions must be reformulated.

5.1.2 Boundary Conditions

The same physical form of the boundary conditions as in Chapter 3 apply to the vortex particle method. However, due to the contribution of the vector velocity potential, $\vec{\Psi}$, the final form of the boundary conditions must be modified to account for the presence of the vorticity.

For rigid surfaces, the no-flux boundary condition is still applied (Equation 3.6), but with the fluid velocity given by Equation 5.1. With the new definition of the velocity, the no-flux boundary condition is expressed as in Equation 5.6. Hence, the source strength given by Equation 3.36 must be modified. The modified source strength when using the vortex particle method is given by Equation 5.7.

$$\hat{n} \cdot \nabla\Phi + \hat{n} \cdot \nabla \times \vec{\Psi} = \hat{n} \cdot \vec{V}_B \tag{5.6}$$

$$\sigma = \hat{n} \cdot \left(\vec{V}_B - \vec{U}_\Psi \right) \tag{5.7}$$

Far away from the body, the fluid velocity remains undisturbed. Following the assumptions from Chapter 3, the influence of the scalar potential field approaches that of a free stream at infinity. This implies that the rotational field generated by the wake must be zero far away from the wake, while the free stream velocity is the gradient of the scalar field.

$$\lim_{\vec{r} \to \infty} \vec{U}_\Psi = 0 \tag{5.8}$$

5.1.3 Body Pressures

Given the presence of the vorticity, the computation of fluid and body pressures must also be modified to account for the vorticity field. Again, following the work of Willis

[59], the Bernoulli equation is applied to the regions with zero vorticity, which includes the entire domain except the localized points represented by vortex particles.

$$-\frac{\nabla P}{\rho} = \frac{\partial \vec{U}_f}{\partial t} + \frac{1}{2}\nabla \left|\vec{U}_f\right|^2 \tag{5.9}$$

The same approach is followed as in Chapter 3, with the exception that the Helmholtz decomposition of the velocity is used. Hence, the pressure gradient is expressed in terms of the scalar and vector potentials:

$$-\frac{\nabla P}{\rho} = \nabla\frac{\partial \Phi}{\partial t} + \frac{\partial(\nabla \times \vec{\Psi})}{\partial t} + \frac{1}{2}\nabla \left|\nabla\Phi + \nabla \times \vec{\Psi}\right|^2 \tag{5.10}$$

The above equation can be integrated along a streamline from a point in the far field ($\vec{r} \to \infty$) to a point on the body surface.

$$-\frac{P}{\rho} = \frac{\partial \Phi}{\partial t} + \int_{\infty}^{\vec{r}_p} \frac{\partial(\nabla \times \vec{\Psi})}{\partial t} d\vec{C} + \frac{1}{2}\left|\nabla\Phi + \nabla \times \vec{\Psi}\right|^2 - \frac{1}{2}\left|\vec{U}_\infty\right|^2 \tag{5.11}$$

As before, the above time derivatives are converted from a Eulerian reference to a Lagrangian reference frame using the material derivative. After substituting the material derivatives and integrating the convective terms, the Bernoulli equation can be rewritten as given in Equation 5.15.

$$\frac{D\Phi}{Dt} = \frac{\partial \Phi}{\partial t} + \vec{V}_B \cdot \nabla\Phi \tag{5.12}$$

$$\frac{D(\nabla \times \vec{\Psi})}{Dt} = \frac{\partial(\nabla \times \vec{\Psi})}{\partial t} + \vec{V}_B \cdot \nabla(\nabla \times \vec{\Psi}) \tag{5.13}$$

$$\frac{P}{\rho} = \frac{1}{2}\left|U_\infty^2\right| + \vec{V}_B \cdot \left(\nabla\Phi + \nabla \times \vec{\Psi}\right) - \frac{1}{2}\left|\nabla\Phi + \nabla \times \vec{\Psi}\right|^2 - \frac{D\Phi}{Dt} - \int_{\infty}^{\vec{r}_p} \frac{D(\nabla \times \vec{\Psi})}{Dt} d\vec{C} \tag{5.14}$$

$$\frac{P}{\rho} = \vec{V}_B \cdot \vec{U}_f - \frac{1}{2}\left|\vec{U}_f\right|^2 + \frac{1}{2}\left|U_\infty^2\right| - \frac{D\Phi}{Dt} - \int_\infty^{\vec{r}_p} \frac{D(\nabla \times \vec{\Psi})}{Dt} d\vec{C} \tag{5.15}$$

Equation 5.15 is the same as given in Chapter 3 for the panel method, with the additional influence of the velocity of the vortex particles. This equation can be evaluated for a given set of vortex particles and surface potentials, with the exception of the last term. This term represents the dynamic pressure resulting from the change in the vorticity. Willis [59] noted that this term can be solved by defining the internal potential, Φ_i, introduced in Chapter 3, such that the velocity induced by the internal potential at the body surface equals the velocity induced by the vortex particles. In this case, the gradient of the internal potential represents the velocity contribution of the vortex particles. Once the internal potential is known, the integral term can be replaced with:

$$\int_\infty^{\vec{r}_p} \frac{D(\nabla \times \vec{\Psi})}{Dt} d\vec{C} = \frac{D\Phi_i}{Dt} \tag{5.16}$$

As stated previously, this work considers only the steady pressure terms. However, for the propeller-ice interaction problem, the unsteady terms are expected to be significant and should be considered at a later date.

5.2 Vorticity Representation

5.2.1 Vortex Particles

Up to this point, no consideration has been given to the specifics of the vector potential, $\vec{\Psi}$. To obtain a Lagrangian numerical method, the vorticity throughout the fluid domain is assumed to be concentrated at discrete points referred to as vortex

particles. Outside of the vortex particles, the fluid is irrotational. The vortex particle representation of the vorticity is given by Winckelmans [60, 61]. The vorticity at a point in the fluid domain is given by Equation 5.17. The strength of the vortex particles is related to the local circulation and the volume of fluid represented by the vortex particle.

$$\vec{\omega}_p\left(\vec{r}_p\right) = \sum_k \vec{\alpha}_k \delta\left(\vec{r}_p - \vec{r}_k\right) \tag{5.17}$$

where,

$\vec{\omega}_p$ - Circulation at the point $\vec{r}_p$

$\vec{r}_p$ - The position of point p in the fluid domain

$\vec{r}_k$ - The position of vortex particle k

$\vec{\alpha}_k$ - The strength of the vortex particle k

The vector potential is then determined from the vortex particle definition using the relationship from Equation 5.2. Once the vector potential is obtained, the rotational velocity component can then be determined by taking the curl of the vector potential.

$$\vec{\Psi}_p = -\sum_k \frac{\vec{\alpha}_k}{4\pi|\vec{r}_{pk}|} \tag{5.18}$$

$$\vec{U}_p = \nabla \times \vec{\Psi}_p = -\sum_k \frac{\vec{r_{pk}}}{4\pi|\vec{r}_{pk}|} \times \vec{\alpha}_k \tag{5.19}$$

5.2.2 Vorticity Kernels

The velocity given by Equation 5.19 is singular at the vortex particle, and produces very high velocities near the vortex. This causes an unrealistic representation of the fluid velocity near the vortex particle, which in turn leads to numerical instabilities

when convecting the vortex particles. Regularized representations of the vorticity are used to eliminate the artificially high velocity in the vicinity of the vortex [61]. This is done by introducing the concept of the Vorticity Kernel. Using a vorticity kernel, Equation 5.19 can be written as:

$$\vec{U}_p = \sum_k \vec{K}(\vec{r}_{pk}) \times \vec{\alpha}_k \tag{5.20}$$

$$\vec{K}(\vec{r}) = -\frac{\vec{r}}{4\pi|\vec{r}|^3} \tag{5.21}$$

The vorticity kernel, $\vec{K}(\vec{r})$, given in Equation 5.21 is known as the Biot-Savart kernel. To obtain a regularized vortex particle method, the Biot-Savart kernel is replaced by alternative representations of the vorticity. Bhagwat and Leishman [5] provide a summary of 2D vortex representations while Winckelmans and Leonard [61] provide several 2D and 3D regularized kernels. The general representation of a 3D regularized kernel is:

$$\vec{K}(\vec{r}) = -\frac{\vec{r}}{4\pi Q\left(\frac{|\vec{r}|}{r_c}\right) r_c^3} \tag{5.22}$$

The parameter r_c is known as the core radius. Winckelmans [60] noted that the influence of the core radius significantly influences the stability of the numerical method. To ensure that the method is numerically stable, the vortex particles must remain sufficiently overlapping throughout the simulation. To ensure that this criteria is met, Winckelmans recommended the core radius be set at 1.3 times the typical distance between vortex particles.

The function $Q(\rho)$ is the regularization function. Winckelmans and Leonard [61] provide several 3D regularization functions. The simplest choice of regularization function is the low order algebraic smoothing, which results in the Rosenhead-Moore

representation of a vortex [29, 31, 50]. Winckelmans [60] suggested the use of a High Order Algebraic kernel due to the fact that closed form analytical diagnostics can be developed that allow the numerical method to be monitored for stability. The regularization function for both are given below. Only the high order algebraic kernel has been used in the current method.

Low Order Algebraic Kernel

$$Q(\rho) = \frac{1}{(\rho^2+1)^{3/2}} \tag{5.23}$$

High Order Algebraic Kernel

$$Q(\rho) = \frac{\rho^2+5/2}{(\rho^2+1)^{5/2}} \tag{5.24}$$

Figure 5.1 compares the high order algebraic kernel to the Biot-Savart kernel for various values of the core radius. The fluid velocity for the Biot-Savart kernel approaches infinity close to the vortex particle. For the regularized vortex kernel, the velocity reaches a maximum at about half the core radius from the vortex particle. Below this, the velocity drops to zero at the vortex particle. Outside of the vortex core, the velocity approaches that of the Biot-Savart kernel.

5.3 Wake Vorticity Representation

5.3.1 Vortex Particle Generation

In the panel method, the wake vorticity is represented as a sheet of dipole panels. The vortex particle method replaces the dipole representation of the wake with vortex particles. Willis [59] used the fact that these representations are analytically equivalent,

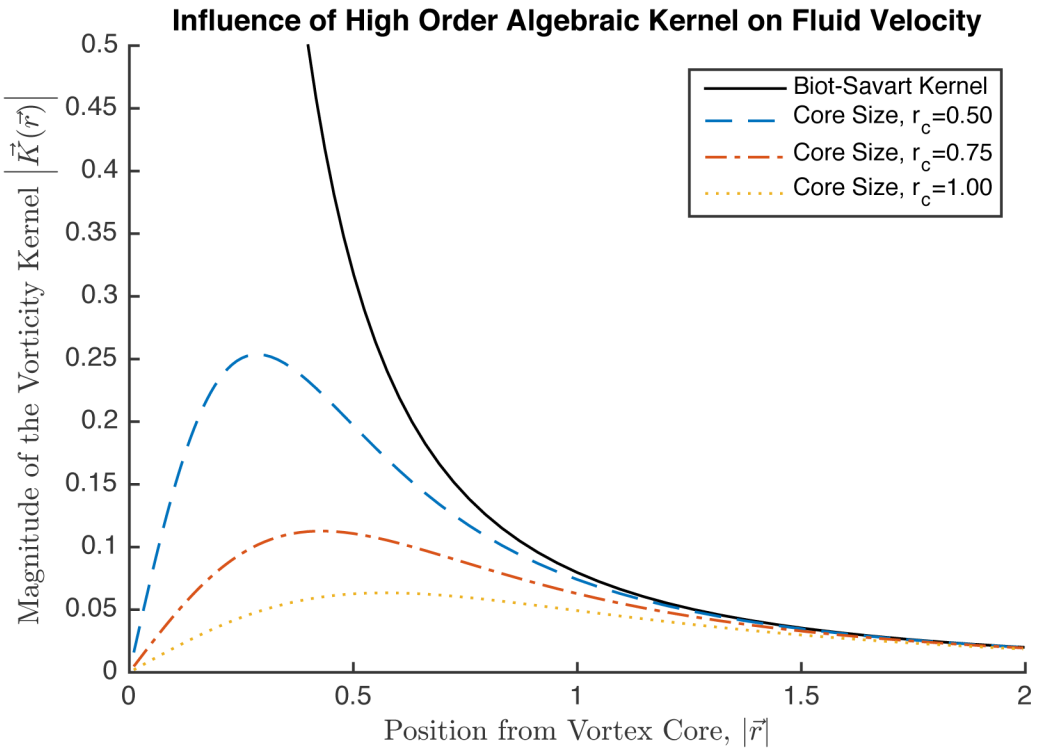

Figure 5.1: Influence of Core Size on Vorticity Kernel.

to develop a numerical method that represented the wake through a combination of panels and vortex particles. Dipole panels are used to represent the near field wake (closest to the body); while in the far field, the dipole panels are replaced by their equivalent vortex particle representation.

This approach allows the benefits of both wake representations to be utilized. The use of dipole panels in the near field allows more accurate computation of pressure at the leading edge and allows the circulation to be related to the Kutta condition as presented in Section 4.4. In the far field wake, vortex particles are used in place of panels to allow for a computationally simpler wake evolution scheme.

The approach used in this work is similar to that of Willis [59]. The process of

generating vortex particles is shown in Figure 5.2. Secondly, the buffer wake is created based on a prescribed geometry. Next, the body position is updated each time step according to its linear and rotational velocities, while the wake panels of the buffer wake are convected with the free stream velocity (note that the induced velocities are ignored for the buffer wake). Next, a new row of buffer wake panels are generated between the previous set of wake panels and the trailing edge of the body. Finally, the last row of wake panels is converted to the numerically equivalent set of vortex particles.

The justification of replacing the vortex panel representation of the wake with vortex particles is based on the numerical equivalency of a dipole and vortex particles. The velocity induced by a vortex panel is equivalent to a ring vortex around the edge of the panel [28]. By considering each side of the panel separately, each can be replaced by a vortex particle with strengths proportional to the length of the panel side as shown in Figure 5.3. The strength of each vortex particle is given by Equation 5.25. For panels sharing a common boundary, the circulation from both panels can be represented using a single vortex particle. The strength of the vortex particle is proportional to the difference in circulation between adjacent panels.

$$\vec{\alpha} \;=\; \Gamma\left(\vec{R}_i - \vec{R}_j\right) \tag{5.25}$$

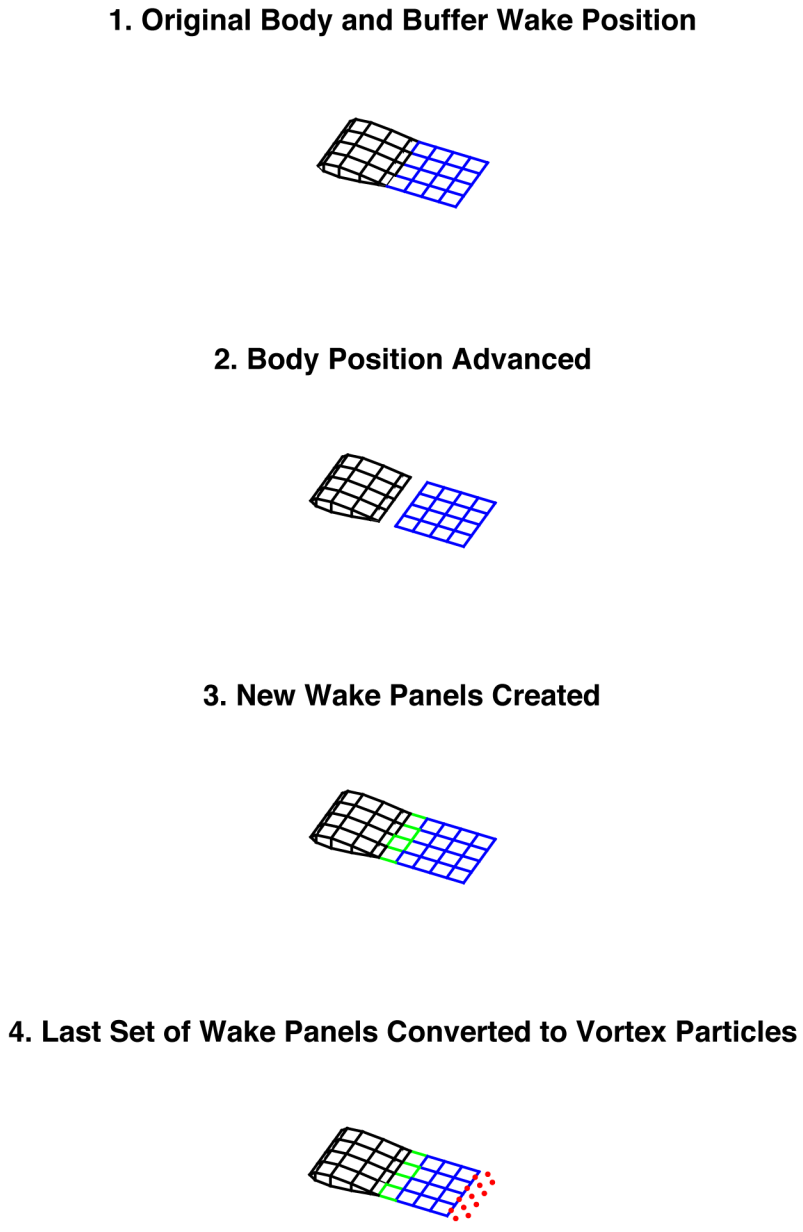

Figure 5.2: Generation of Vortex Particles.

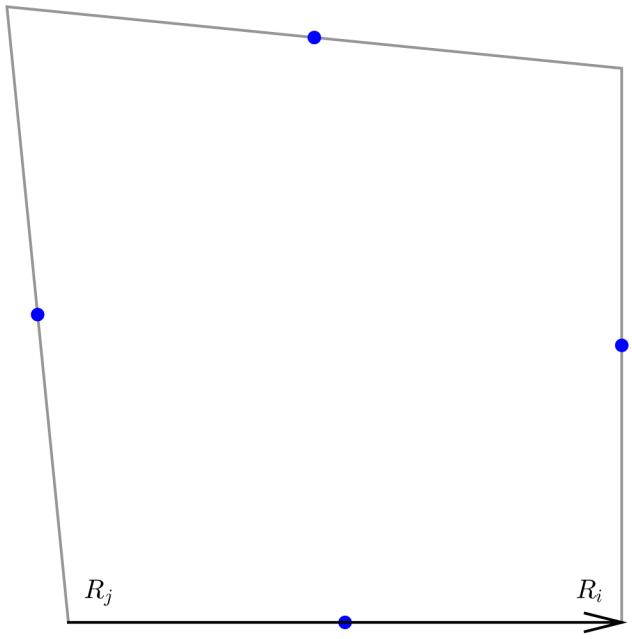

Figure 5.3: Location of Equivalent Set of Vortex Particles for a Dipole Panel.

5.3.2 Vortex Evolution

To update the wake, a time stepping algorithm is required. Each time step, the position and strength of each vortex particle is updated based on evolution equations for position and circulation. The positions of the vortex particles are updated based on the local fluid velocity, while the strength of each particle is updated to account for the stretching of the vorticity as given by Equation 5.4. This is analogous to the deformation of the geometry of wake panels in the panel method. Three different schemes are possible to solve the vorticity equations: the classical scheme, the transpose scheme, or the mixed scheme [60]. Although each is analytically equivalent, they represent different numerical approaches. Winckelmans recommended the use of transpose scheme as it is the only one which conserves the total vorticity, hence, it has been adopted for this work. The evolution equations for the transpose scheme are given by:

$$\frac{d}{dt}\vec{x}^p(t) = \vec{U}_f\left(\vec{x}^p(t), t\right) \tag{5.26}$$

$$\frac{d}{dt}\vec{\alpha}^p(t) = \left(\vec{\alpha}^p(t) \cdot \nabla^T\right)\vec{U}_f\left(\vec{x}^p(t), t\right) \tag{5.27}$$

Winckelmans provides a closed form analytical solution for the stretching term for High Order Algebraic kernels [60]. However, as discussed by Calabretta [8], in a mixed panel and vortex particle method, both evolution equations must account for the presence of the panels. The position evolution equation depends on the local fluid velocity, while the strength evolution depends on the gradient of the fluid velocity. The fluid velocity used in the evolution equations must be the total velocity given as the superposition of the velocity contribution from the panels and the vortex particles based on the Helmholtz decomposition. Calabretta has provided analytical solutions

for the velocity gradient due to constant strength source and dipole panels, as well as their multipole expansions [8]. These gradients must be superimposed with the gradients from the vortex particles for use in Equation 5.27.

5.3.3 Local Particle Refinement

As the particles are convected with the fluid velocity they will tend to concentrate in areas with negative velocity gradients and space out in areas with positive gradients. This creates an uneven distribution of particles within the wake, and leads to areas of the wake where particle cores no longer overlap, which is required for a well formed vortex particle method. Velocity gradients will also cause vortex particles to stretch according to Equation 5.27. As a vortex particle stretches, it increases in strength. As the vortex particles are discrete representations of a continuous vortex, the stretching artificially concentrates vortices at a single point. Cottet provides a thorough discussion of the issues associated with nonuniform spatial distributions of particles in Lagrangian methods [11].

For the above reasons, it is occasionally necessary to refine the locations and strengths of the vortex particles. Various grid based approaches have been proposed in the literature and are discussed by Cottet [11]. These methods generally work by using the vortex particles to compute the circulation at fixed locations corresponding to a grid in the fluid domain. New vortex particles are then created at the grid nodes, which replace the original vortex particles. The replacement of vortex particles ensures that vortex particles remain evenly spaced while adequately representing the original fluid circulation.

As discussed in the introduction, methods based on creating grids in the fluid domain are not well suited to the propeller application due to the complexities of developing a suitable grid. In addition, grid based methods would have a tendency to alter the location of the particles close to the body's trailing edge, influencing the accuracy of the Kutta condition.

As the goal of this work was to develop a numerical method that does not required a grid in the fluid domain, a particle refinement scheme that is not dependent on the construction of a grid is desirable. Mansfield proposed such an approach that was based on tracking the total distortion of each vortex particle by stretching three initially orthogonal vectors according to the evolution equations [20]. Once either one of the vectors was stretched past an acceptable limit, the vortex particle is split into two particles along the direction of the distortion. By appropriately setting the length of the initial vectors, and comparing these to the particle core size, the particles can be split in such a way as to maintain particle overlap, without requiring knowledge of adjacent particles or using a grid.

Mansfield noted that the splitting algorithm has the effect of generating a large number of vortex particles. Hence, he also suggested a method for combining vortex particles which are sufficiently close together. Cottet notes that the scale that can be resolved by the vortex particle method is related to the core radius that is selected and not the spacing between particles [11]. Hence, combining particles as proposed by Mansfield does not influence the resolution of the results, but serves to reduce the number of particles and reduces the computation effort.

5.4 Summary

In the current implementation, the near field wake is modelled using dipole panels as discussed in Chapter 4. Currently, the geometry of the near field wake is specified a priori and no attempt is made to align the near field wake with the local fluid velocity. The strength of the dipole circulations is calculated using the iterative pressure kutta scheme.

In the far field, vortex particles are used in place of dipole panels. Each time step, a new panel is constructed near the trailing edge and the previous panel is converted into vortex particles based on the numerical equivalency between a dipole panel and a ring vortex. Each vortex particle has a strength that is related to the size of the vortex panel and the circulation calculated using the Kutta condition from the previous time step. The vortex particles are then updated using the RK3 algorithm used by Calabretta [8].

Using an approach based on a combined vortex particle and panel method, the challenges associated with convecting and maintaining a well-defined wake are overcome. The next chapter presents some validation cases and uses them to highlight the benefits and challenges of the combined panel and vortex particle method.

Chapter 6

Results

This chapter presents several validation cases. The first case is the simple solution of the flow around a sphere. This serves to verify that the basic panel method portion of the code is functioning as expected, including the computation of influence coefficients and the numerical velocity gradient. The second validation case is the evolution of a vortex ring. This example uses only the vortex particle method, without the coupling to the panel method, thus, the results serve to verify the evolution of vortex particles.

The next two cases are for wings of differing geometries. The first case is a rectangular wing with a known two dimensional solution. By increasing the aspect ratio of the wing, one can compare the results at the midspan to the analytical solution. This serves to validate the kutta condition. The second wing is a circular profile, which has been commonly used for verification by other researchers. The circular wing adds complexity over the rectangular wing due to the more complex geometry and the significant influence of the wake rollup on the midspan.

The method is then applied to a marine propeller operating in the bollard condi-

tion. This case is more challenging than the wings due to the rotational motion and the presence of multiple blades.

6.1 Panel Method Verification

The sphere was chosen for verification of the panel method as it has a known analytical solution. The solution for the potential flow around a sphere is based on the potential due to a single dipole aligned with the inflow, and located at the centre of the sphere. For a dipole located at the origin with a uniform inflow velocity aligned with the x-axis, the velocity potential is given by Equation 6.1. The strength of the dipole can be determining by applying the appropriate boundary conditions such that the velocity at the stagnation point is zero. The resulting potential for a sphere of radius, R, in a uniform inflow aligned with the x-axis, U, is given by Equation 6.1. On the body of the sphere, the velocity potential can be seen to be linear with respect to the horizontal position and independent of either the transverse or vertical directions.

$$\Phi = Ux + \frac{\mu x}{4\pi r^3} \tag{6.1}$$

$$\Phi = Ux\left[1 + \frac{1}{2}\left(\frac{R}{r}\right)^3\right] \tag{6.2}$$

Based on the potential around the sphere, other physical values can be determined. The velocities in each component can be determined by differentiating the velocity potential with respect to the appropriate direction. The velocities in each of the principle Cartesian directions are given in Equation 6.3 through Equation 6.5. It can be shown from the equation that a zero velocity is recovered when using the coordinates of either stagnation point. Also, the maximum velocity occurs on the y-z

plane and has a value of 1.5 times the free stream velocity.

$$V_x = U\left\{1+\frac{1}{2}\left(\frac{R}{r}\right)^3-1.5\left(\frac{x}{r}\right)^2\left(\frac{R}{r}\right)^3\right\} \tag{6.3}$$

$$V_y = -U\left(\frac{xy}{r^2}\right)\left(\frac{R}{r}\right)^3 \tag{6.4}$$

$$V_z = -U\left(\frac{xz}{r^2}\right)\left(\frac{R}{r}\right)^3 \tag{6.5}$$

Furthermore, the pressure on the surface of the sphere can be determined using Bernoulli's Equation for steady potential flow. Substituting the velocity equations into the Bernoulli's Equation and non-dimensionalizing using the pressure coefficient, a simple expression can be determined for the non-dimensional pressure on the body's surface (Equation 6.6). Based on this equation, it can be seen that the pressure coefficient on the body of the sphere ranges from unity to -1.25. Values less than zero indicate that the velocity is accelerating around the body creating a drop in pressure. Positive values indicate a decelerated fluid flow and hence an increase in pressure.

$$C_p = \frac{P}{\frac{1}{2}\rho U^2} = 1 - 2.25\sin^2\theta \tag{6.6}$$

The numerical results of the panel method have been computed for a sphere consisting of 400 panels (Figure 6.1). The results have been compared against the analytical results in Figure 6.2. The results show that the numerical model provides excellent correlations with the analytical results. This verifies that the fundamental panel method functions as expected, including the influence coefficients and the numerical velocity gradient on the surface.

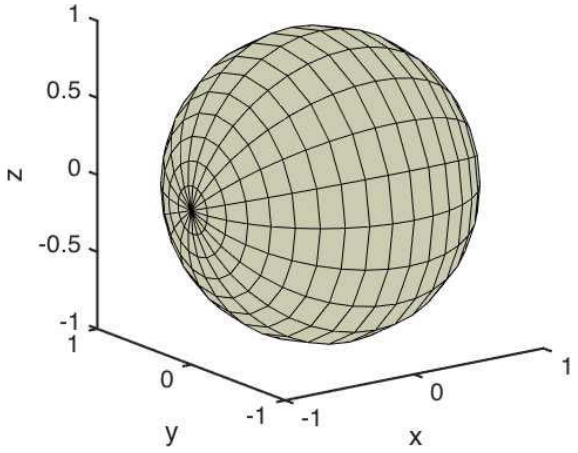

Figure 6.1: Panel Arrangement of the Sphere

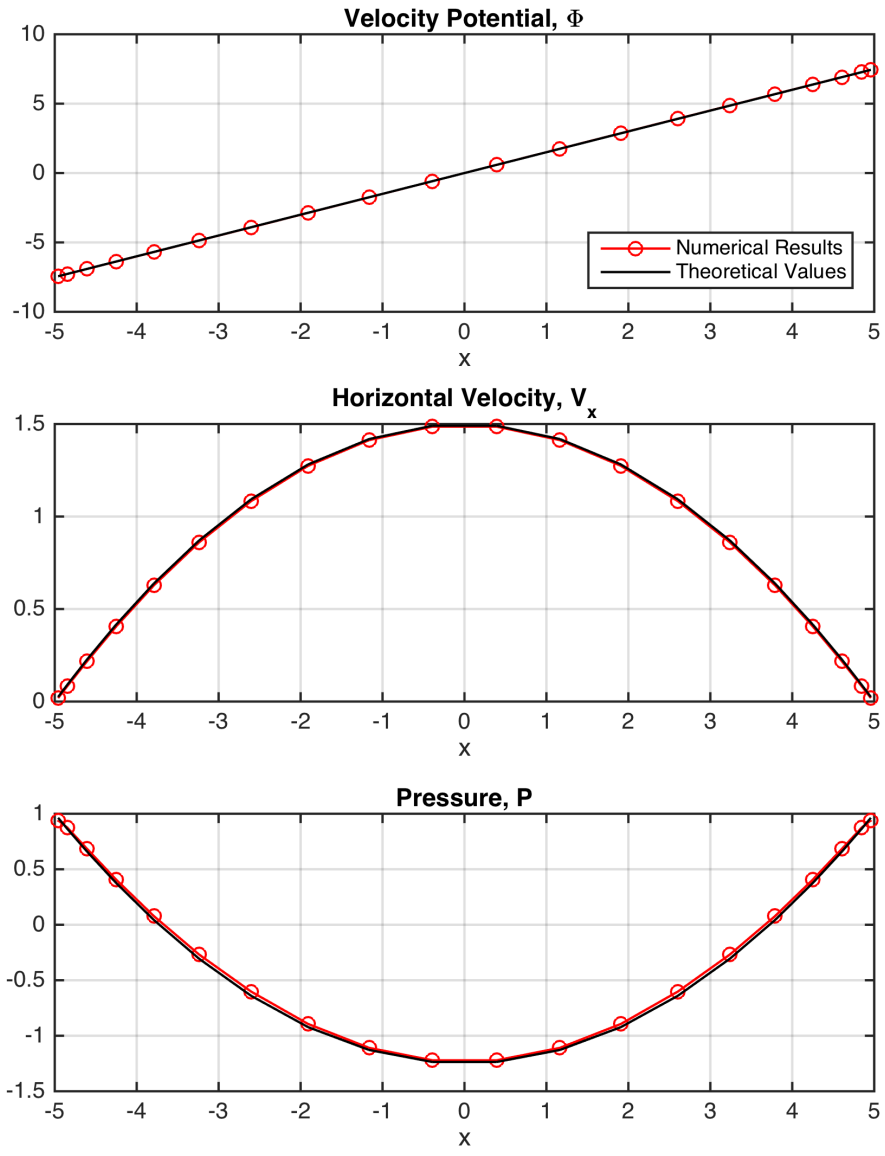

Figure 6.2: Comparison of Panel Numerical Results for Sphere with Radius R=5 and Uniform Inflow U=1

6.2 Vortex Particle Method Verification

To verify the vortex particle method, the single inviscid ring vortex problem presented by Winckelmans has been replicated [60]. The viscous version of this problem has also been used for verification by Calabretta [8]. The reader is referred to the work of Calabretta for the details of the particle discretization and strength assignment, which is not repeated here.

To be consistent with the work of Calabretta and Winckelmans, a vortex ring of radius of $R = 1$ was used. The vortex was discretized into $N_\phi = 80$ circumferential sections, each consisting of 81 vortex particles, corresponding to four radial sets of particles ($n_c = 4$). The core radius was set to 0.100. For this particular application, the axisymmetric nature of the problem is utilized to minimize the computational effort.

The diagnostics developed by Winkelmans [60] at the beginning of the simulation are shown in Table 6.1. The results are similar to those obtained by both Winckelmans and Calabretta [8, 60]. The linear impulse, I, is slightly higher than that obtained by Winckelmans, but closer than that obtained by Calabretta. Both energy diagnostics, E and E_f, are significantly closer to Winckelmans. As noted by Calabretta, the equation for exact enstrophy, ϵ, provided by Winckelmans appears to have an error, so no value is obtained. The approximate enstrophy, ϵ_f, is only slightly higher than both Winckelmans and Calabretta. Overall, the initial diagnostics are considered within an acceptable range. Calabretta provides some possible reasons for the differences that do exist.

The vorticity after 3.5 seconds is plotted for one section of the vortex ring in Fig-

Table 6.1: Comparison of the Initial Diagnostics for the Vortex Ring Problem

	Winckelmans [60]	Calabretta [8]	Current Method
n_c	4	4	4
N	6,480	6,480	6,480
$I(0)$	3.214	3.133	3.274
$E(0)$	1.0476	1.0128	1.0407
$E_f(0)$	1.0476	1.0129	1.0408
$\epsilon(0)$	61.35	N/A	N/A
$\epsilon_f(0)$	62.38	63.38	63.52

ure 6.3. The vorticity shows slight differences from that presented by Winckelmans [60]. However, the overall nature of the vortex ring and the magnitudes of the vorticity are similar. The results are considered sufficiently close to those presented by Winckelmans for the present purpose. Hence, it can be concluded that the evolution of the vortex particles has been verified.

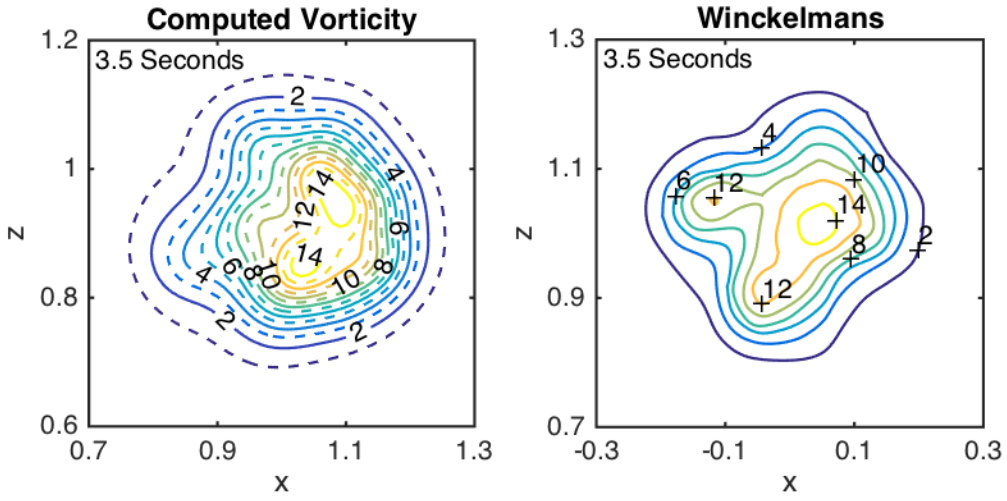

Figure 6.3: Comparison of Vortex Ring Vorticity with Winckelmans [60]

Note: Location and orientation of vortex rings differ

6.3 Rectangular Wing

The next case that has been selected for verification is that of a rectangular wing. This case has been selected to ensure the accuracy of the Kutta condition. The wing profile selected is a Van de Vooren symmetric profile. The geometry of the profile as well as the exact solution for a 2D flow over the foil is presented by Dragos [12].

To allow the comparison of the 3D solution with the exact 2D solution, various aspect ratio wings have been selected. First, a wing of aspect ratio 5 (10 units tip to tip, with a chord length of 2 units) has been modelled as shown in Figure 6.4. The wing has been discretized into 21 span wise panels and 20 chord wise panels. Linear spacing is used in the span wise direction, while cosine spacing is used in the chord wise direction to provide adequately small spacing near the tip and trailing

edge with a reasonable number of panels. The solution has been allowed to run for 25 seconds in 0.5 second time steps. The resulting velocities on three sections are shown in Figure 6.5. The middle section shows reasonable correspondence with the exact 2D solution given the finite aspect ratio of the wing. Sections closer to the tip show higher discrepancy due to the increased crossflow on the wing. The difference between the velocity on the top and bottom of the wing near the trailing edge is zero for all sections. The verifies that the pressure Kutta Condition has been correctly implemented.

To determine convergence with the exact solution, wings of aspect ratios 10, 20 and 40 were also used for verification. These wings were developed by adding additional panels for each section without changing the panel size, hence increasing the wing length. This requires more panels for higher aspect ratio wings. The horizontal and vertical velocity components, along with the velocity magnitudes for the middle section are shown in Figure 6.6 for all aspect ratios. The results show that the solution converges at an aspect ratio of around 20. The solutions for higher aspect ratio wings are closer to the exact solution than the lower aspect ratio wing, but fail to model the peak pressure. This is likely a result of the low number of panels at the leading edge combined with the curvature of the wing, reducing the accuracy of numerical gradient used to compute the velocities.

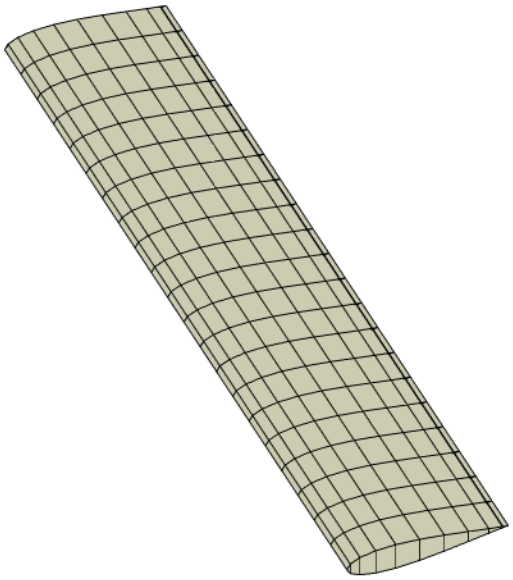

Figure 6.4: Van de Vooren Wing Geometry (AR = 5)

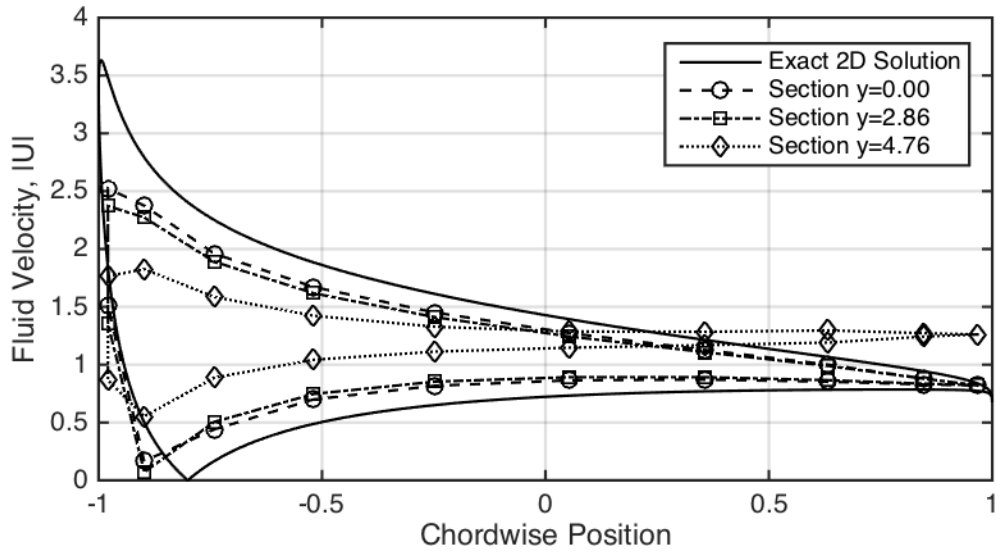

Figure 6.5: Fluid Velocity at Different Section for Van de Vooren Wing (AR = 5)

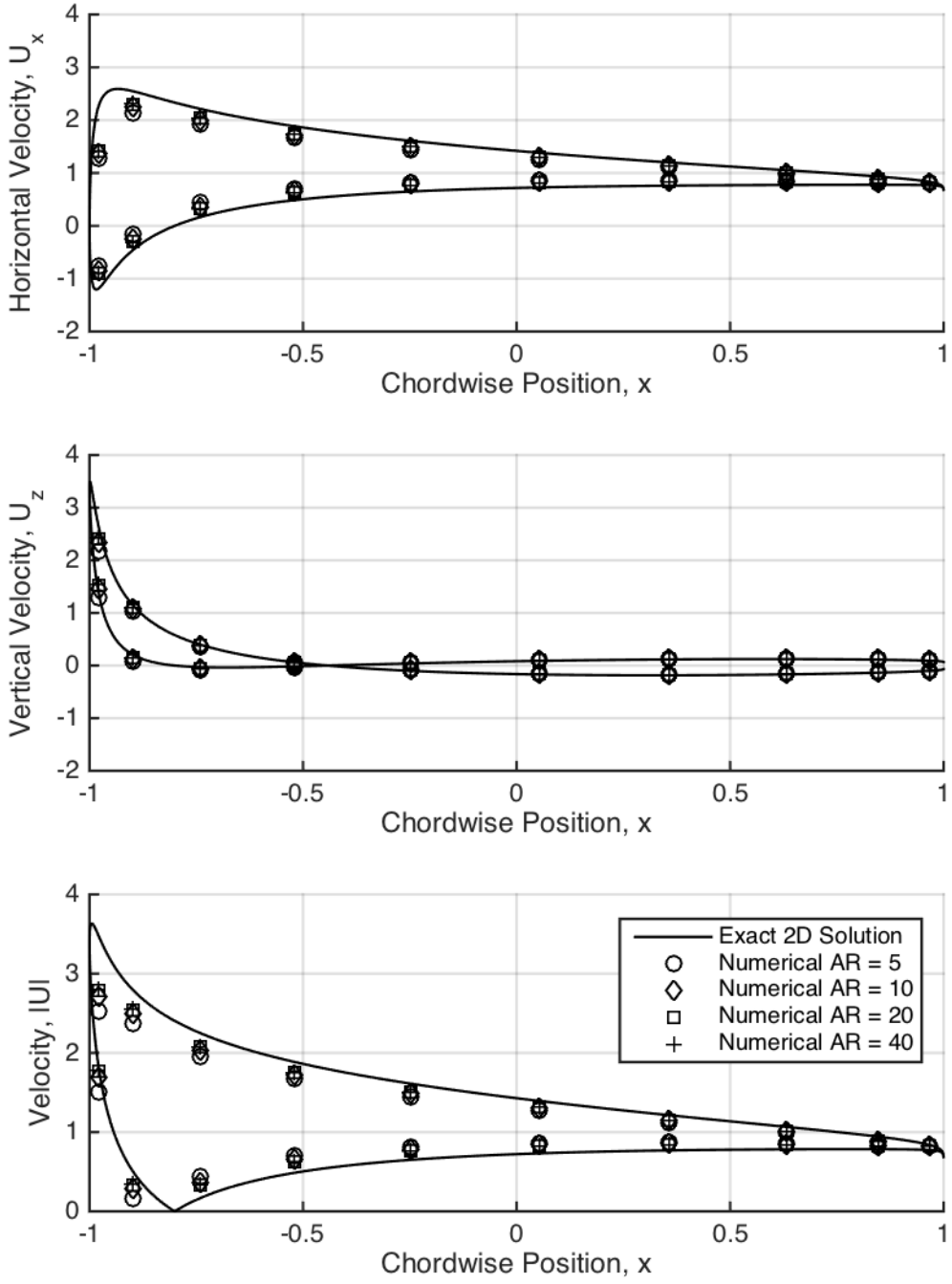

Figure 6.6: Fluid Velocity at Mid Section ($y = 0$) for Van de Vooren Wing

6.4 Circular Wing

A circular wing with unit radius is modelled to ensure that the method is capable of accurately modelling cases with strong cross flows. Initial attempts at modelling the circular wing using rectangular spacing failed to converge due to the complexity of modelling the flow around the tip. To rectify this problem, a blade orthogonal grid as used by Pyo was implemented [47]. This grid produces panels that are less distorted near the tip, improving the numerical stability of the method.

Two profiles have also been considered. First, a simple elliptical profile has been considered. Secondly a NACA 0010 profile has been modelled following the work of Kim [26]. The geometry of the circular wing with elliptical profile for thickness to diameter ratio, e, of 0.05 is shown in Figure 6.7.

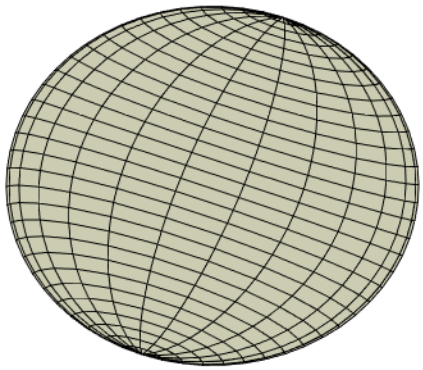

Figure 6.7: Geometry of Circular Wing with Thickness Ratio of $e = 0.05$

The calculation was run for 5 seconds at time steps of 0.1 seconds. To verify that the results were suitably converged, a time series of circulation has been plotted in Figure 6.8 for the NACA 0010 section. The results show that the model is both stable, as well as suitably converged on the solution after 50 time steps.

The location of the vortex particles after 5 seconds is shown Figure 6.9, along with cross sections of the fluid vorticity, computed based on the vortex particle strengths and locations. The tip vortex has caused the particles to rollup near the edges of the wake. In addition, the starting vortex created at the beginning of the problem due to the impulsive start has caused the far end of the wake to roll up. Although the wake would continue to evolve with additional time steps, the influence of the starting vortex on the wing is sufficiently small after 50 time steps, and the solution near the wing has reached a steady state.

To verify that the Kutta Condition is converging on the correct results, the circulation, Γ, determined from the model is compared to that of the exact solution for the section lift coefficient determined by Jordan [21] for a flat circular plate. The section lift coefficient (Equation 6.7) can be related to the circulation through the Kutta–Joukowski theorem (Equation 6.8).

$$c_l = \frac{l}{\frac{1}{2}\rho U_\infty^2 s} \tag{6.7}$$

$$l = \rho U_\infty \Gamma \tag{6.8}$$

$$\Gamma = \frac{1}{2} c_l U_\infty s \tag{6.9}$$

where, c_l is the section lift coefficient,

l is the section lift,

ρ is the fluid density,

U_∞ is the free stream velocity,

s is the chord length,

Γ is the circulation.

The results are plotted in Figure 6.11 for an elliptical wing section with various thickness coefficient, e, as well as for a NACA 0010 section. The results for the thin elliptical cross section as well as the NACA 0010 section show good correspondence with the circulation near the middle of the wing. Close the wing tips, the circulation is higher than the solution given by Jordan. Ramsey obtained a similar solution using a panel representation of the wake with rollup [48]. Ramsey accredited the differences between Jordan's analytical solution and the numerical results to the wake rollup. As such, the results obtained for the thin elliptical section and the NACA 0010 are considered suitable solutions despite not matching the results by Jordan. The wings using thick elliptical cross sections ($e = 0.05$ and $e = 0.10$) show lower circulation values across the entire length of the wing. This is a direct result of the thickness of the wing.

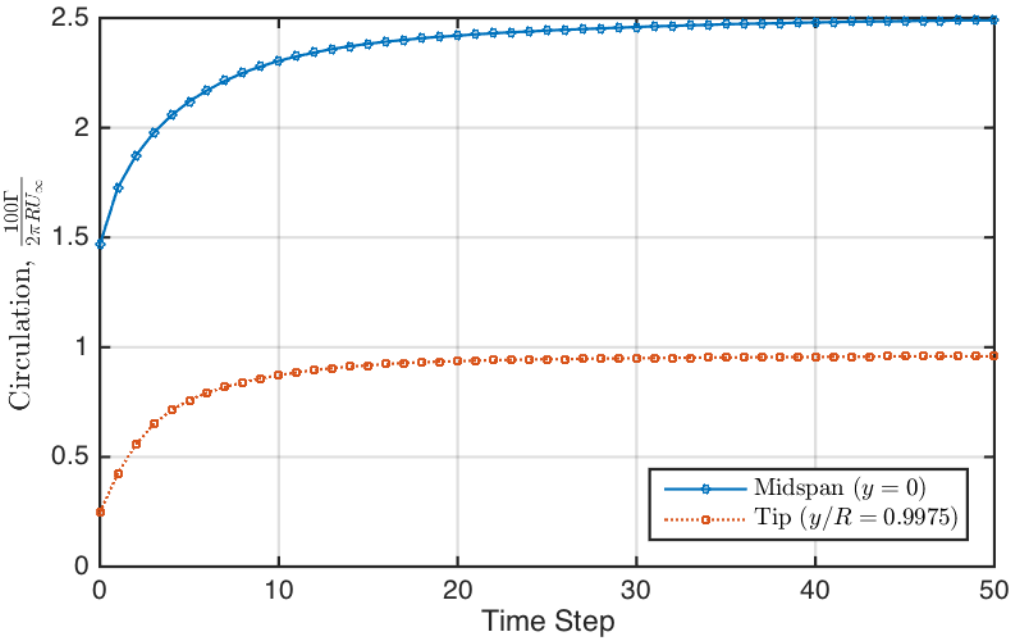

Figure 6.8: Time Series of Circulation for Circulation Wing ($e = 0.05$)

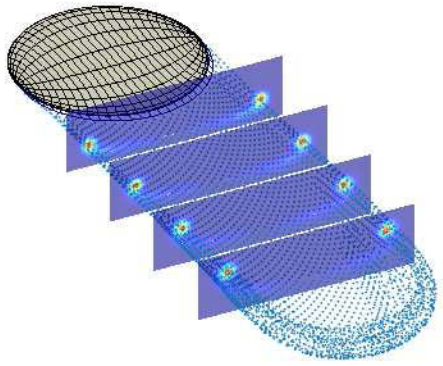

Figure 6.9: Resulting Wake after 5 seconds ($e = 0.05$)

Slices show circulation calculated from resulting vortex particles

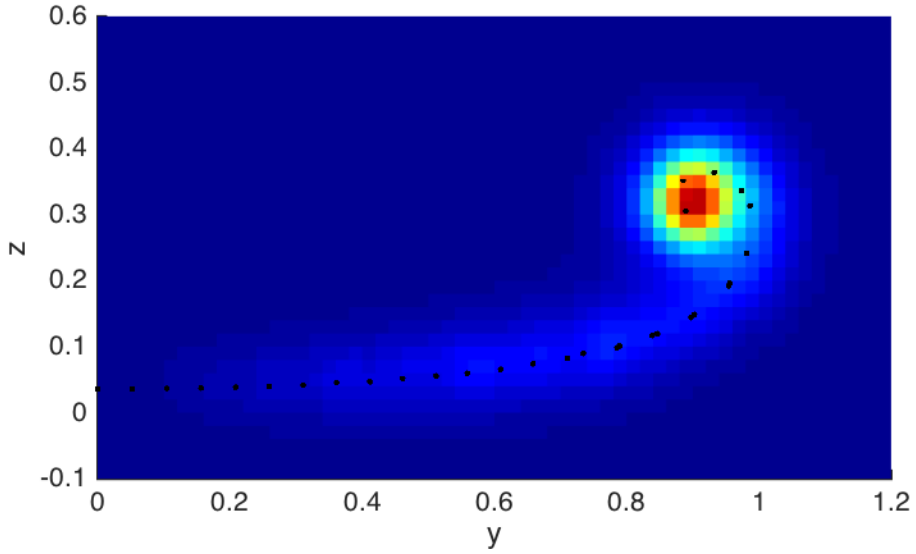

Figure 6.10: Cross Section of Circulation at $x = 3.5$ after 5 seconds ($e = 0.05$)

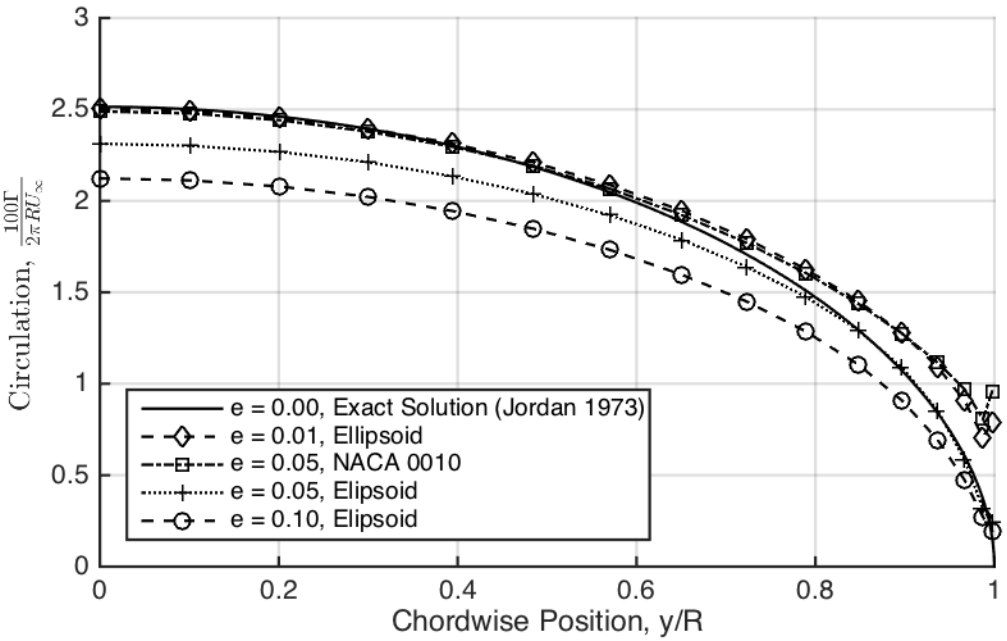

Figure 6.11: Circulation for a Circulation Wing with 5° Angle of Attack

6.5 B4-70 Propeller

The code has been applied to a marine propeller. A B-Series propeller was selected due to the readily available geometry information [10] as well as published thrust and torque coefficients for a range of geometries [30]. The selected propeller was four bladed, with an expanded area ratio of 0.7 (B4-70). The pitch ratio selected was 0.7. The problem was scaled using a propeller diameter of 1 m and rotational speed of 1 rps.

A blade orthogonal panel arrangement similar to that used for the circular wing was used to generate the panels on the blades. 10 panels were used in the radial direction and 8 per side of the blade were used in the chord wise direction, for a total of 160 panels per blade. The resulting panel arrangement is shown in Figure 6.12.

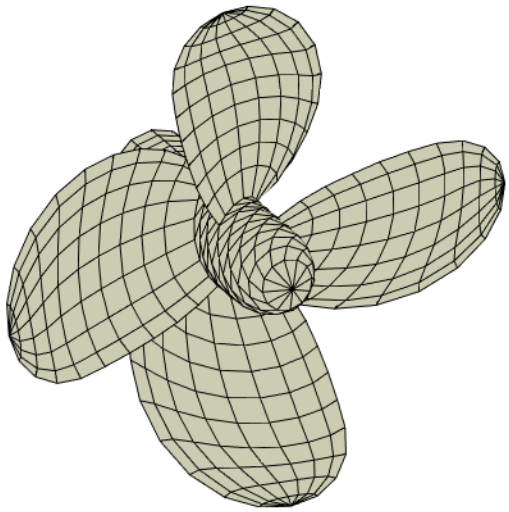

Figure 6.12: Panelized Geometry of B4-70 Propeller

In the case of the wing problems discussed above, a short buffer wake consisting of a single set of panels was used. For the propeller problem, a large buffer wake consisting of 11 panels has been used, representing half of a propeller revolution. The buffer wake is created at the beginning of the problem with a fixed pitch. The pitch is fixed at 0.7 and is not modified throughout the simulation. This acts to move the generation of vortex particles farther downstream from the panels, eliminating the close coupling between the panel method used to determine the circulation, and the vortex particle method. Having the vortex particles shed farther downstream prevents vortex particles from being generated near the hub surface, where velocities can become large near the edge of the panels.

The influence of the size of the buffer wake on the circulation at the start of the simulation is shown in Figure 6.13. The circulations have been calculated at the first time step, prior to the generation of vortex particles. For buffer wakes with between 2 and 4 panels, the pressure kutta condition does not converge, due to the strong influence of the starting vortex on the adjacent blade. The strength of the starting vortex with 11 buffer wake panels is considerably less than with a single panel, and continues to slowly decrease as more buffer panels are added.

The simulation is advanced using time steps of 0.05 seconds. This produces wake panels that are approximately 0.157 long near the tip of the propeller. This provides a maximum distance between vortex particles, which is used as the criteria for selecting the core radius used in the vortex particle kernel. The core radius is set at a value of 0.2, giving an overlap ratio of about 1.27 at the tip. Near the root, the overlap ratio is increased to 4.6 where particles are closer spaced due to the smaller panels generated by the slower speed close to the centre of rotation.

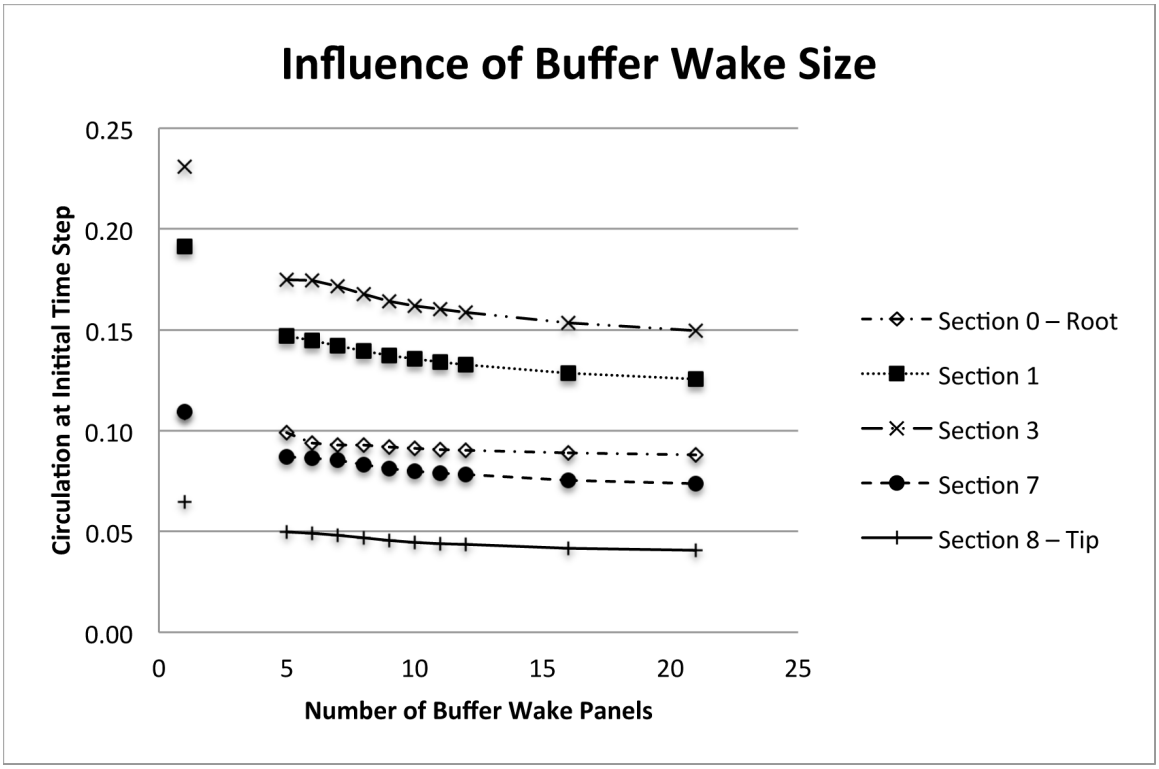

Figure 6.13: Influence of Buffer Wake Size on Circulation

Using the above inputs, the simulation becomes unstable after 20 time steps (1 second). The location of the vortex particles after 4, 8, 12 and 16 time steps is shown in Figure 6.14. Note that after approximately 0.5 seconds, vortex particles have been convected back towards the propeller. The numerical instability is a result of these vortex particles interacting with the wake panels. As the velocity is singular near the panel edges, the problem becomes unstable if a vortex particles comes too close to the edge.

The behaviour above is a result of the particle refinement algorithm. Splitting of vortex particles near the root vortex causes vortex particles to be created in areas of high velocity gradients, which are then convected backwards due to the influence of

the root vortex.

The simulation was repeated without the the vortex refinement scheme. In this case, the simulation remains stable up to time step number 95 (4.75 seconds). The evolution of the vortex particles up to 4.5 seconds is shown in Figure 6.15. Without the refinement scheme, vortex particles in the starting vortex are stretched due to the self-induced velocity. This stretching continues throughout the simulation until the strength of the vortex particles causes high velocities on neighbouring particles. This leads to numerical instabilities in the Runge-Kutta solver used to convect the particles.

Reasons for the numerical instabilities, along with possible solutions to overcome these challenges are discussed in the next chapter.

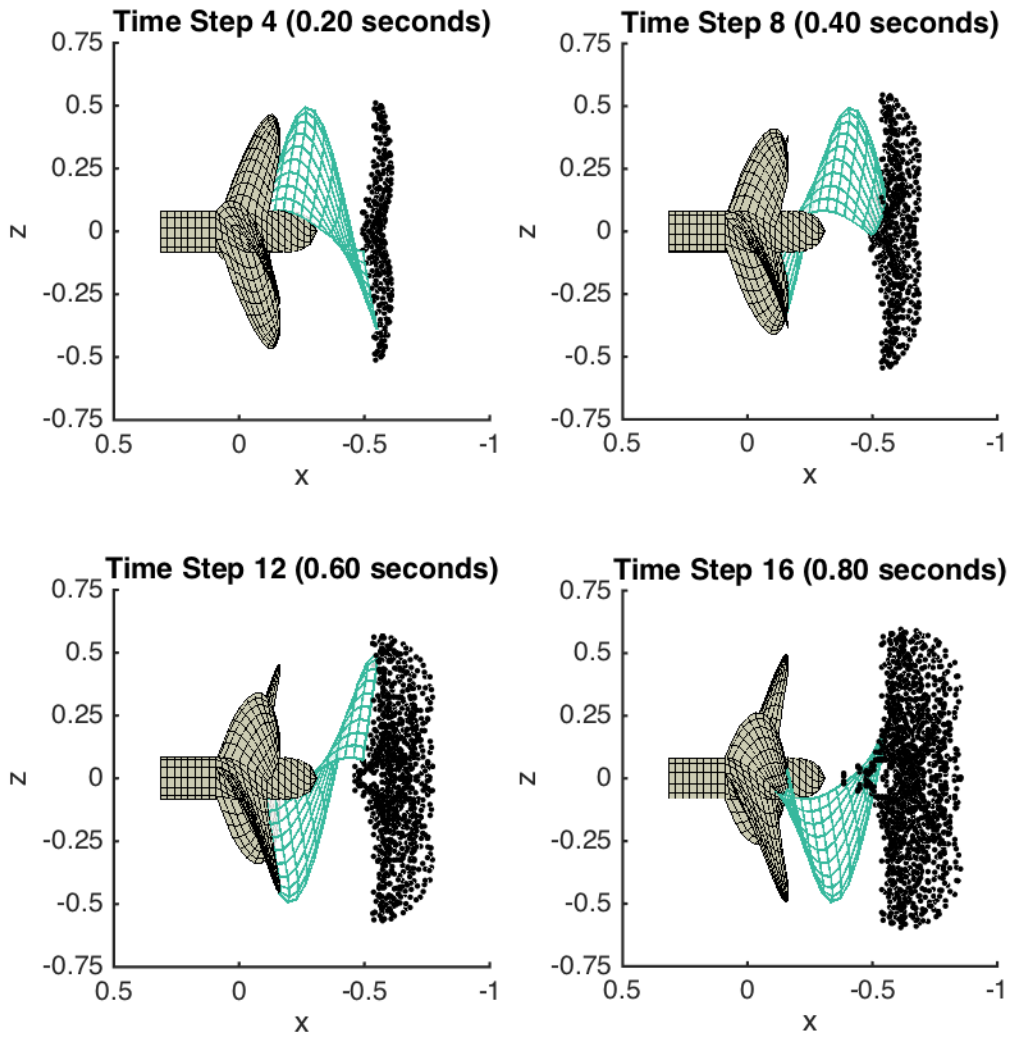

Figure 6.14: Wake evolution using particle refinement scheme

Note: Only one near field wake shown

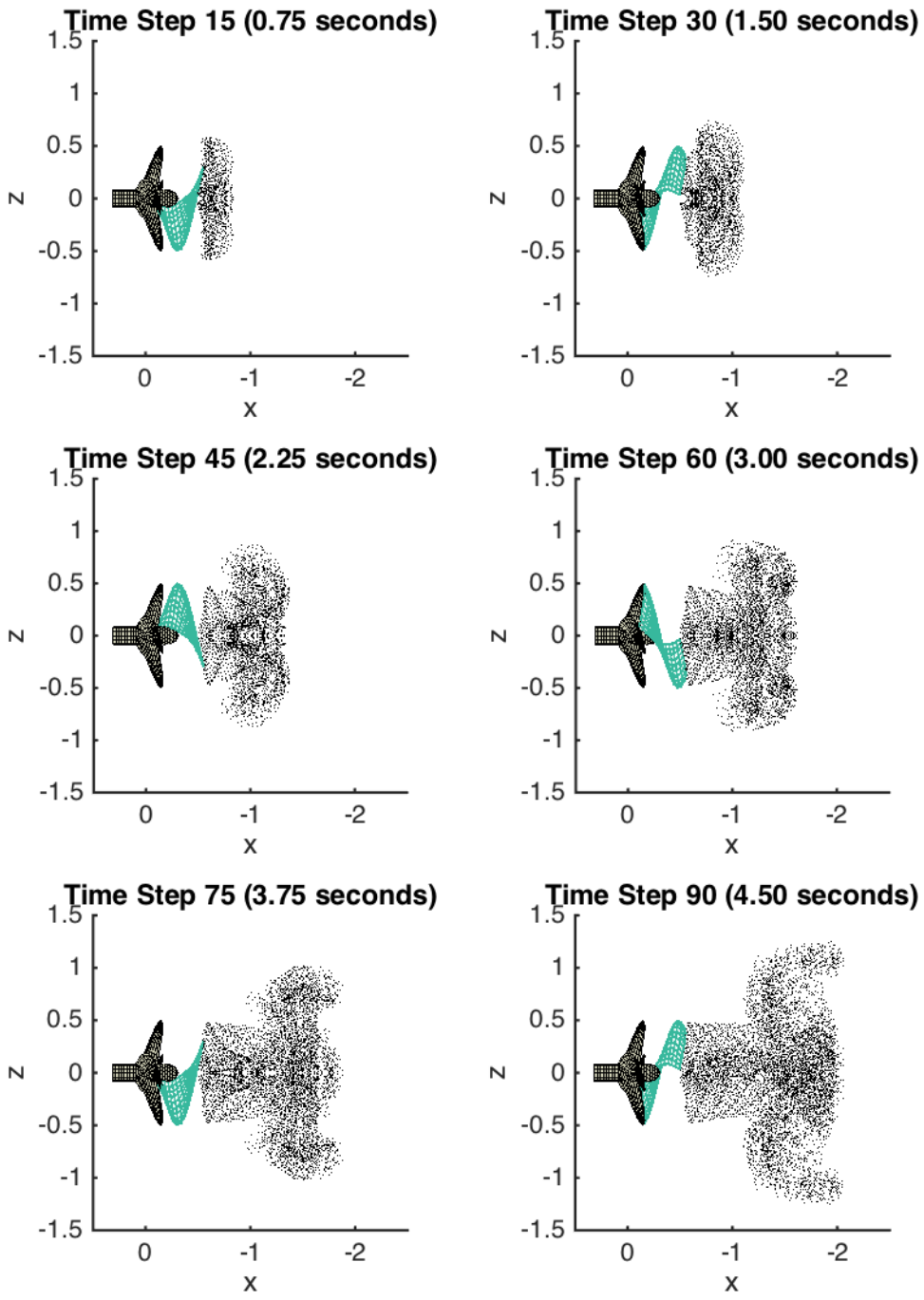

Figure 6.15: Wake geometry without refinement scheme after 4.5 seconds

Note: Only one near field wake shown

Chapter 7

Discussion

7.1 Current Challenges

The results presented in the previous chapter indicate that a coupled panel method and vortex particle method is sufficient for resolving the lift and modelling the wake behind a wing. However, the rotation of the propeller, combined with the presence of wakes from multiple blades adds increased complexity over the wing problem. The nature of the problem leads to strong velocity gradients in the wake region, particularly near the propeller hub. These gradients lead to instability in the numeric methods used for the evolution equations of the vortex particles, which depend both on the velocity and its gradient.

The particle splitting algorithm suggested by Mansfield [20] is able to successfully maintain overlap in the wake behind wings, and maintain the physical appearance expected based on the panelized approach of the panel method. However, the interaction between the vortices shed at the root of the propeller blades cause significant

stretching in this region. The splitting algorithm generates vortex particles near the centerline of the propeller, which are convected by the root vortex back toward the propeller. This behaviour causes the algorithm to be very sensitive to the choice of cut-off values used in the particle refinement scheme.

When applied without particle refinement, the method is able to resolve realistic behaviour near the hub, as indicated by the flow of particles downstream as expected based on the induced velocity. However, the lack of splitting algorithm leads to unrealistic growth of the strength of vortex particles in the starting vortex. This leads to extremely high velocity gradients in the vicinity of the vortex particles, which further leads to instability when other vortex particles are sufficiently close.

These challenges arise due to the lack of ability to model the details of the root vortex at the scale required to capture the behaviour of the flow. According to Cottet [11], the scale of the flow that can be resolved depends on the core radius selected. Therefore, in order to obtain sufficient numerical resolution, the core radius must be reduced, which in turn requires that the spacing of the particles be reduced to achieve sufficient particle overlap.

In the current method, the spacing of the vortex particles is directly related to the size of the wake panel in which the vortices are generated. This is required as the vortices are created from the edges of the panel. The size of the wake panel is in turn related to the size of both the time step and the propeller panels. Hence, decreasing the particle spacing requires that both the number of panels used in the propeller representation is increased and that the time step is reduced.

The ability to reduce the resolution is limited by the numerical efficiency of the method. Each time step requires the computation of the velocity at the centroid of

each panel and at each vortex particle. For the convection of the vortex particles with the Runge-Kutta method, the velocity calculation is required three times for each vortex particle. The computation time required to compute the velocity also increases proportionally with the number of panels and vortex particles. The ability to run the simulation on a consumer grade computer within acceptable time scales limits the number of the panels and vortex particles, placing practical limits on the resolution that can be achieved.

7.2 Potential Solutions

Various improvements are possible in order to overcome these challenges. First, improvements to the computational efficiency of the velocity are possible. Far field assumptions have already been applied to reduce the cost of computing the influence of panels on points far away. Similar methods have been developed to reduce the cost of velocity calculations for vortex particles [31]. These methods work by grouping particles into clusters and computing the velocity at points far away from the cluster using approximate formulations. Computational effort is required to develop the cluster, but the cluster can be reused for a large number points, reducing the overall computational effort.

Particle clustering techniques would serve to reduce the computational time, allowing the number of panels and particles to be increased while staying within reasonable computation times. Lindsay reports that the computation time can be reduced by a factor of 5 to 10 for 50,000 particles depending on the level of acceptable error [31]. Even with the particle clustering algorithms, the resolution of the vortex

particle method still depends directly on the number of panels and the size of the time step. Hence, the particle spacing cannot be reduced without requiring increased computational costs in all elements of the method.

The second improvement possible is the use of higher order panels methods. This would eliminate the dependency of the particle resolution on the panel resolution and time step. Willis used the fact that the fluid vorticity is equal to the gradient of the dipole strength to generate vortex particles [59]. In the constant panel method, the dipole strength is non-continuous, which leads to the vorticity being concentrated at the edge of the dipole panels. Willis used a higher order panel method based on quadratic basis functions to develop a smooth representation of the dipole strength on the wake panels. Using this representation, the vortex particles can be generated at arbitrary locations on the panels. Hence, the location and spacing of the particles can be generated independent of the size of the panels.

The above result is highly beneficial to the application of rotating bodies. The tip of the propeller blade moves significantly faster than the root. Hence, for a constant time step, the distance swept out by the trailing edge is larger at the tip. This leads to unequal sizing of the wake panels along the span of the blade. In the current method, this leads to uneven spacing of vortex particles, with particles being more closely spaced near the root.

A higher order panel method would allow for the spacing of vortex particles to be selected independent from both the size of the time step and the size of the panels on the propeller. As the current application is not directly interested in the accuracy of the solution on the propeller, a low panel resolution could be utilized while still maintaining a sufficiently high resolution in the wake to resolve the flow near the hub.

The application of high order panels would have the additional benefit of eliminating the singularity that exists at the edge of the constant strength panel. The singularity at the edge of the constant strength panel leads to high velocities and velocity gradients at the panel edges. This restricts the location of vortex particles, which cannot be located near the panels. This is problematic when parts of the body are downstream of the wake generating edges, such as the hub's fairing cone. The use of higher order panel methods may allow for the elimination of the extended near field wake required in this method to prevent vortex particles from being created on the hub.

7.3 Future Application to Icebreaking

Provided the above challenges can be overcome, the proposed method can be applied to the icebreaking problem introduced in Chapter 2. Either additional panels or the modified Green's function must be added to account for the ice surface. This ensures that there is no fluid flow through the ice surface. The pressures can then be computed using the Bernoulli equation.

To apply the Bernoulli equation, the unsteady terms should be included. This requires the calculation of the internal potential to obtain the dynamic pressure term resulting from the vortex particles.

Finally, an ice mechanics model would need to be applied to predict the breaking phenomenon. The ice sheet acts as a plate on a dynamic foundation. Analytical solutions for stress in the ice field are available for a circular patch load [37]. The ice mechanics problem could therefore be solved by superimposing multiple patch loads.

The patch loads can be obtained directly from the values of pressure computed from the Bernoulli formula. More complex ice geometries would need more advanced ice mechanics models to predict breaking.

The model could also be used to predict ice clearing of ice floes or icebergs. The forces on the ice could be computed by a combination of the pressure, as well as by utilizing a skin friction coefficient to account for the viscous drag. The total force on an ice can be determined by numerically integrating the pressures and drag forces.

7.4 Additional Applications

In addition to the application to icebreaking, which formed the original basis for this thesis, the method proposed has applications in other fields where the downstream wake from lifting bodies is of interest. In the marine field, the downstream wake from propellers is of interest in other subject areas. For instance, Liu studied the effect of downstream propeller wake from DP vessels on the various submerged equipment used in the offshore industry [44]. Downstream propeller wake can also influence civil engineering structures [41, 52]. The accuracy of such studies could be improved by considering the induced rotational velocity induced due to the propeller rotation.

Vortex particle methods have already been applied in the aviation industry to study the behaviour of aircraft wings [56, 59]. Calabretta also used vortex particle methods to study the influence of an aircraft engine on the downstream wing [8, 9]. This study used an actuator disk in place of a rotating propeller or turbine. Using the techniques presented in this thesis, it may be possible to improve upon the work of Calabretta to account for the induced rotational components of the flow.

Another area where this work could be applied is to helicopter rotors. Opoku has already demonstrated the application of vortex particles to helicopter rotors [43]. The application of vortex particles to helicopter rotors allows for the interaction of the wake with downstream components, including the modelling of ground effect.

A final area where this work could be applied is in energy industry for the modelling of wind turbines. Wind turbines are typically installed in wind farms, where the influence of a single turbine influences downstream turbines [40]. These influences can have a significant impact on the power that can be generated. The approach presented in this thesis could allow for a more accurate representation of the downstream wake.

Chapter 8

Conclusions

For this work, a low order three dimensional panel method suitable for application to lifting surfaces has been developed based on the work of various M.I.T. researchers [28, 19]. In the current implementation, the geometry of the wake panels must be pre specified. This limits the applicability of the code as, in general, the wake location is unknown and must be solved as an integral part of the solution such that the wake is aligned with the flow.

An attempt has been made at implementing an arbitrary three dimensional wake alignment scheme based on the work of Pyo [47]. However, this approach was deemed ill-suited to the current application of interest, which requires that the wake geometry be modelled far downstream of the propeller, as well as being allowed to interact and become deformed by the presence of the ice sheet. The development of this approach was therefore abandoned in favour of alternate approaches.

Vortex particle methods were identified as a potentially viable alternative to panel methods. Willis and Calabretta have successfully combined vortex particle meth-

ods with panel methods to applications in the aeronautics industry [8, 59]. Based upon these approaches and the work of Winckelmans [60], an inviscid vortex particle method was developed and coupled with the low order panel method.

The methods were successfully applied to wing problems using rectangular and circular wings. The results showed good correlation with those presented by other researchers. In addition, the vortex particle wakes showed realistic behaviour that was capable of capturing the rollup of the wing tip vortex.

The application to the propeller problem failed to converge and led to numerical instabilities. This prevented full application to the icebreaking problem identified as the motivation for this work. The differences between the propeller problem and the wing problems that were investigated that lead to the challenges encountered are as follows:

- Since, the rotational motion causes the tip of the propeller to move faster than sections near the hub, vortex particles shed near the tip of the propeller are spaced farther apart than vortex particles close to the root. In the current work, this has been addressed by selecting of the core radius such that sufficient overlap is available at the tip. This causes a large amount of overlap in the particles near the root.

- The wake shedding algorithm places vortex particles close to the hub of the propeller. The evaluation of the velocity at particles near the hub is therefore highly influenced by the edges of the panels used to model the hub. Due to the singularities at the edges of the panels, a buffer wake is required such that vortex particles are not created until downstream of the hub.

- The rotational nature of the problem combined with presence of multiple blades increases the amount of interaction between the vortex particles, particularly at the blade root. These interactions involve strong velocity gradients that require a fine resolution in order to resolve.

The last item above was not possible to overcome within the scope of this thesis. Practical limitations on numerical efficiency restrict the scale that can be resolved using regularized vortex particles.

This work has demonstrated that panel methods alone are not suited to the computation of the downstream wake field of marine propellers. Although it is possible to model the wake far enough downstream for the application of propeller design, there are practical difficulties related to the connectivity of the wake. Vortex particle methods show promising results for computing the complex flow in the wake field. However, there are challenges that must be overcome before a fully coupled panel method and vortex particle code can be applied to the marine propeller problem. The use of particle clustering algorithms and higher order panel methods are expected to alleviate many of the challenges faced in the current work. Provided these challenges can be overcome, combined vortex particle and panel methods are expected to be a viable technique to predict the breaking of ice using propeller wake.

Chapter 9

Recommendations

Particle clustering algorithms, that reduce the computational effort of computing the velocity induced by vortex particles, are required for the practical application of vortex particle methods. The large number of vortex particles required to model the fluid flow in the wake of a marine propeller leads to extremely slow computations when performed directly. This makes even modest calculations unviable on todays consumer grade computers.

High order panel methods are also recommended for any application requiring the coupling between vortex particles and panel methods. Flat panels with constant strength have singularities at the panel edges that cause numerical instability if calculations are required near the edges. However, the largest limitation for the coupled method is that the generation of vortex particles is restricted to the edges of the wake panels. High order panels would allow vortex particles to be spaced at even intervals, hence allowing a more stable method without requiring large numbers of panels.

Once the above improvement are made, the particle refinement scheme requires

additional attention. Optimum values for the cut-off parameters need to be established such that realistic flow behaviour is maintained, while utilizing a minimum number of vortex particles.

Bibliography

[1] Ashby, D. L. Potential flow theory and operation guide for the panel code pmarc_14. Tech. Rep. TM-1999-209582, NASA, Dec. 1999.

[2] Ashby, D. L., Dudley, M. R., and Iguchi, S. K. Development and validation of an advanced low-order panel method. Tech. Rep. TM-101024, NASA, 1988.

[3] Banerjee, P. K., and Butterfield, R. *Boundary Element Methods in Engineering Science*. McGraw-Hill Book Company (UK) Limited, Maidenhead, Berkshire, England, 1981.

[4] Barrett, R., Berry, M., Chan, T. F., Demmel, J., Donato, J., Dongarra, J., Eijkhout, V., Pozo, R., Romine, C., and der Vorst, H. V. *Templates for the Solution of Linear Systems: Building Blocks for Iterative Methods*, 2nd edition ed. SIAM, Philadelphia, PA, 1994.

[5] Bhagwat, M. J., and Leishman, J. G. Generalized viscous vortex model for application to free-vortex wake and aeroacoustic calculations. In *AHS International Forum 58* (June 2002), American Helicopter Society.

[6] Brebbia, C. A. *The boundary element method for engineers.* Pentech Press, London, 1978.

[7] Brebbia, C. A., Telles, J. C. F., and Wrobel, L. C. *Boundary Element Techniques: Theory and Applications in Engineering.* Springer-Verlag, Berlin, Heidelberg, 1984.

[8] Calabretta, J. *A Three Dimensional Vortex Particle-Panel Code for Modelling Propeller-Airframe Interaction.* PhD thesis, California Polytechnic State University, June 2010.

[9] Calabretta, J., and McDonald, R. A three dimensional vortex particle-panel method for modeling propulsion-airframe interaction. In *48th AIAA Aerospace Sciences Meeting* (2010).

[10] Carlton, J. 6 - propeller performance characteristics. In *Marine Propellers and Propulsion (Second Edition)*, J. Carlton, Ed., second edition ed. Butterworth-Heinemann, Oxford, 2007, pp. 87 – 135.

[11] Cottet, G.-H., and Koumoutsakos, P. *Vortex Methods: Theory and Practice.* Cambridge University Press, 2000.

[12] Dragos, L., and Dinu, A. A direct boundary integral method for the three-dimensional lifting flow. *Computer Methods in Applied Mechanics and Engineering 127* (1995), 357–370.

[13] Ferrieri, J. M., Veitch, B., and Akinturk, A. Experimental study on ice management through the use of podded propeller wash. In *Third International Symposium on Marine Propulsors* (May 2013), pp. 26–33.

[14] Gaggero, S., and Brizzolara, S. Exact modeling of trailing vorticity in panel method for marine propeller. In *2nd Internation Conference on marine research and transportation* (Ischia, Naples, Italy, June 2007).

[15] Gamma, E., Helm, R., Johnson, R., and Vlissides, J. *Design Patterns: Eleemtns of Reusable Object-Oriented Software*. Addison-Wesley, 1994.

[16] Greeley, D. S., and Kerwin, J. E. Numerical methods for propeller design and analysis in steady flow. *SNAME Transaction 90* (1982).

[17] He, C., and Zhao, J. Modeling rotor wake dynamics with viscous vortex particle method. *AIAA Journal 47*, 4 (April 2006), 902–915.

[18] Hess, J. L., and Smith, A. M. O. Calculation of nonlifting potential flow about arbitrary three-dimensional bodies. *Journal of Ship Research 8*, 2 (Sept. 1964), 22–44.

[19] Hsin, C.-Y. *Development and Analysis of Panel Methods for Propellers in Unsteady Flow*. PhD thesis, Massachusetts Institute of Technology, Sept. 1990.

[20] John R. Mansfield, O. M. K., and Meneveau, C. Towards lagrangian large vortex simulation. *ESAIM: Proceedings 1* (1996), 49–64.

[21] Jordan, P. F. Exact solutions for lifting surfaces. *AIAA Journal 11*, 8 (August 1973), 1123–1129.

[22] Keinonen, A., and Martin, E. Ice management experience in the sakhalin offshore with azimuth icebreakers. In *Icetech* (2008).

[23] Keinonen, A., and Martin, E. Natural breaker drillship / fpso concept for ice offshore. In *Icetech* (Banff, Canada, July 2008).

[24] Kerwin, J. E. Marine propellers. *Annual Review of Fluid Mechanics 18* (1986), 367–403.

[25] Kerwin, J. E., Kinnas, S. A., Lee, J.-T., and Shih, W.-Z. A surface panel method for the hydrodynamic analysis of ducted propellers. In *Transactions*, vol. 95. SNAME, 1987, pp. 93–122.

[26] Kim, G.-D., Lee, C.-S., and Kerwin, J. E. A b-spline based higher order panel method for analysis of steady flow around marine propellers. *Ocean Engineering 34* (2007), 2045–2060.

[27] Kinnas, S., Hsin, C.-Y., and Keenan, D. A potential based panel method for the unsteady flow around open and ducted propellers. In *Eighteenth Symposium on Naval Hydrodynamics* (1991).

[28] Lee, J.-T. *A Potential Based Panel Method for the Analysis of Marine Propellers in Steady Flow.* PhD thesis, Massachusetts Institute of Technology, July 1987.

[29] Leonard, A. Computing three-dimensional incompressible flows with vortex elements. *Annual Review of Fluid Mechanics 17* (1985), 523–559.

[30] Lewis, E. V., Ed. *Resistance, Propulsion and Vibration*, second ed., vol. II of *Principles of Naval Architecture*. Society of Naval Architects and Marine Engineers (SNAME), 1988, ch. 8.

[31] Lindsay, K., and Krasny, R. A particle method and adaptive treecode for vortex sheet motion in three-dimensional flow. *Journal of Computational Physics 172* (2001), 879–907.

[32] Lohi, P., and Savikurki, J. Azimuth thrusters in icebreakers: A revolutionary step ahead. In *International Shipbuilding Conference (ISC)* (St. Petersburg, Russia, October 1994).

[33] Martin, E. Ahti ice trials - March 4th, 2007. Confidential, AKAC Inc, 2007.

[34] Martin, E. Fennica ice trials – March 7th to 9th, 2007. Confidential, AKAC Inc, 2007.

[35] Martin, E., Keinonen, A., and Brown, H. Ice management effectiveness predictions. In *Icetech* (2008), SNAME.

[36] Maskew, B. Program vsaero theory document: A computer program for calculating nonlinear aerodynamic characteristics of arbitrary configurations. Contract Report 4023, NASA, Sept. 1987.

[37] Michel, B. *Ice Mechanics*. Les Presses De L'Université Laval, 1978.

[38] Morino, L. Subsonic potential aerodynamics for complex configurations: a general theory. *AIAA Journal 12*, 2 (1974), 191–197.

[39] Morino, L., Chen, L.-T., and Suciu, E. Steady and oscillatory subsonic and supersonic aerodynamics around complex configurations. *AIAA Journal 13*, 3 (1974), 368–374.

[40] Newman, J., Lebron, J., Meneveau, C., and Castillo, L. Streamwise development of the wind turbine boundary layer over a model wind turbine array. *Physics of Fluids 25* (August 2013).

[41] Nielsen, B. C. Bowthruster-induced damage: A physical model study on bowthruster-induced flow. Master's thesis, Delft University of Technology, June 2005.

[42] Nyman, T., Riska, K., Soininen, H., Lensu, M., Jalonen, R., Lohi, P., and Harjula, A. The ice capability of the multipurpose icebreaker botnica - full scale trials. In *Port and Ocean Engineering under Arctic Conditions (POAC)* (1999), vol. 2, pp. 631–643.

[43] Opoku, D. G., Triantos, D. G., Nitzsche, F., and Voutsinas, S. G. Rotorcraft aerodynamic and aeroacoustic modelling using vortex particle methods. In *23rd Congress of International Council of the Aeronautical Sciences* (September 2002).

[44] Pengfei Liu, Neil Bose, S. L. Numerical and experimental modeling of dynamic positioning for offshore systems. Tech. rep., Petroleum Research Atlantic Canada, May 2003.

[45] Politis, G. K. Simulation of unsteady motion of a propeller in a fluid including free wake modeling. *Engineering Analysis with Boundary Elements 28* (2004), 633–653.

[46] Press, W. H., Teukolsky, S. A., Vetterling, W. T., and Flannery, B. P. *Numerical Recipes in C++*, second ed. Cambridge University Press, 2002.

[47] Pyo, S. *Numerical Modeling of propeller tip flows with wake sheet roll-up in three dimensions*. Phd, Massachusetts Institute of Technology, July 1995.

[48] Ramsey, W. D. *Boundary integral methods for lifting bodies with vortex wakes*. Phd, Massachusetts Institute of Technology, May 1996.

[49] Rolls Royce. 50 years of azimuth thrusters. *In Depth 24* (2015), 25–27.

[50] Rosenhead, L. The spred of vorticity in the wake behind a cylinder. *Proceedings of the Royal Society A: Mathematical, Physical and Engineering Sciences 127*, 806 (June 1930), 590–612.

[51] Ruijters, D., van Scheltinga, J. T., ter Haar Romeny, B. M., and Suetens, P. Design pattern for multi-modality coordinate spaces. In *10th Philips Software Conference* (Veldhoven (the Netherlands), November 2006).

[52] Schokking, L. Bowthruster-induced damage. Master's thesis, Delft University of Technology, June 2002.

[53] Segletes, S. B., and Walters, W. P. A note on the application of the extended bernoulli equation. Tech. Rep. ARL-TR-1895, Army Research Labratory, February 1999.

[54] Suciu, E., and Morino, L. Nonlinear steady incompressible lifting-surface analysis with wake roll-up. *AIAA Journal 15*, 1 (1977), 54–58.

[55] Takinaci, A. C., Atlar, M., and Korkut, E. A practical surface panel method to predict velocity distribution around a three-dimensional hydrofoil including boundary layer effects. *Ocean Engineering 30* (2003), 163–183.

[56] Wilis, D. J., Peraire, J., and White, J. K. A combined pfft-multipole tree code, unsteady panel method with vortex particle wakes. *International Journal for Numerical Methods in Fluids 53* (2007), 1399–1422.

[57] Wilkins, J. R. Propeller design optimization for tunnel bow thrusters in the bollard pull condition. Master's thesis, Massachusetts Institute of Technology, June 2012.

[58] Williamson, J. H. Low-storage runge-kutta schemes. *Journal of Computational Physics 35* (1980), 48–56.

[59] Willis, D. J. *An unsteady, accelerated, high order panel methods with vortex particle wakes*. PhD thesis, Massachusetts Institute of Technology, June 2006.

[60] Winckelmans, G. *Topics in vortex methods for the computation of three- and two-dimensional incompressible unsteady flows*. PhD thesis, California Institute of Technology, Pasadena, California, February 1989.

[61] Winckelmans, G., and Leonard, A. Contributions to vortex particle methods for the computation of three-dimensional incompressible unsteady flows. *Journal of Computational Physics 109* (1993), 247–273.

[62] Yu-min, S., and Sheng, H. Prediction of hydrodynamic performance of marine propellers by surface panel method. *Journal of Marine Science and Application 1*, 1 (June 2002), 9–15.

Appendix A

Application Code Details

The program implementation developed for this work has been funded by industry supporters, which has guided the requirements for the program developed. First, the code must be able to be ran by private industry, free of commercial restrictions. Secondly, the code is intended to be run on personal computers. This allows the code to be assessable without the use of high powered supercomputers.

To achieve the first objective, the panel and vortex particles methods have been developed from the ground up, with minimal reliance on third party libraries. The code has been developed using the C++11 programming language, using the GNU Autotools to coordinate the build process. Object orientated programming techniques have been used to ensure that the code is modular, allowing for easy interchangeability of numerical algorithms, which can be configured without modifying the main panel method code.

All programming and testing has been performed on a 2.4 GHz Intel Core i7 MacBook Pro with 8 GB ram and a 2.93 GHz Intel Core i7 personal computer with 8

GB ram, running Ubuntu 12.04. Use of multi-threading has been made where possible to take advantage of the added efficiency available with the multiple core architecture available on both development systems.

Three libraries have been developed for this work, EHMgeo, EHMsci, and AKACim.

The EHMgeo library has been developed specifically to ease the handling of multiple coordinate systems within the code. Separate coordinate systems are required for the local panel coordinate system, the propeller fixed co-ordinate system, as well as the global coordinate system. Tracking the coordinate system of each variable within the code quickly becomes cumbersome. Using the design pattern presented by Ruijters [51], it has been possible to attach coordinate systems to each three dimensional point and vector. The library automatically keeps track of the coordinate system of each variable, and implicit handles coordinate system conversions when performing operations between points and vectors of different coordinate systems. When a point or vector is required in a specific required coordinate system, the user can request the conversion into a coordinate system of choice. This library simplifies the overall code development and eliminates the need to explicitly transform coordinates throughout the code.

The EHMsci library has been developed to isolate the numerical routines required throughout this work. The fundamental data structures used by the library are vector and matrix classes, which allow for the storage of data in a manner suitable for performing linear algebra calculation. Basic operations such as addition, subtraction, scalar multiplication, etc., are possible for both data types. The library also has built in functionality for:

- Solving system of linear equations,
- Computation of eigen vectors and values,
- Solutions to ordinary differential equations, and
- Root finding of multi-dimensional equations.

The AKACim library is the main library performing panel and vortex panel method calculations. The library handles the reading of configuration input files and geometry files, the panel method and vortex particle calculations, and the writing of outputs. For each application of the code, a separate application is wrote, which uses the libAKACim library. The code is configurable in the following ways:

- Algorithm Selection - Various panel method algorithms such as the source method, direct method, morino kutta condition, pressure kutta condition, etc., have been programmed as different classes. The choice of panel method is selected by the user of the library.
- Strategy Design Patterns - Various algorithms, such as those in the libEHMsci library, have been programmed using strategy design pattern [15]. The strategy design pattern allows the user of the library to customize the panel method by selecting various numerical algorithms used; including the algorithm to solve the system of linear equations, and the multi-dimensional root finder used by the pressure kutta condition.
- Configuration File - The various parameters used in the model are adjusted by a configuration file, which is loaded at run-time. The configuration file allows

for the fine tuning of the numerical methods, such as the vortex particle core radius, size of the time step, length of the buffer wake, number of iterations, fluid inflow, as well as the scale and position of the propeller or wing body. The configuration file is in the form of a MS Windows ini file (attribute-value pairs), which is read using the SimpleIni library, provided under the MIT license.

- Object Geometry - The object geometry is provided in a custom formatted file. The geometry is provided as an ordered list of points to be used as panel nodes, followed by a list of panels, given by either three or four nodes. The wake generating edges are specified as a list of nodes, connected along the trailing edge of the lifting body. Various algorithms have been generated in Matlab to generate geometry files based on the type of body and the parameters that define the object.

To solve the system of linear equations given by Equation 4.9, either the BiConjugate Gradient method (BiCG) [4] or LU Decomposition method [46] is used. The BiCG method is an iterative method which can compute the solution of dense non-symmetric matrices. LU Decomposition is an exact method, which is effective at determining the solution of equations of the form $AX = B$, for multiple vectors B, as long as the matrix A remains unchanged. In the case of pressure kutta condition, Equation 4.9 must be solved at each iteration of the root finding algorithm. At each iteration, the influence matrices remain unchanged, allowing the LU Decomposition to remain unchanged, such that the solution can be efficiency computed each time step with different values for the circulation. In addition, due to the nature of the root finding algorithm, accurate solutions for the system of linear equations is required for

small changes in circulation. Hence, the exact solution of the LU Decomposition is desirable over the BiCG method, which may lead to instabilities in the root finding algorithm if no improvement to the solution is seen due to small changes in the circulation.

For the pressure kutta condition, it is necessary to solve for the circulation which produces zero pressure difference along the trailing edge. To achieve this, a multi-dimensional root finder is required. For this work, Broyden's Method has been used [46]. Broyden's Method is globally convergent and does not require the computation of the Jacobian matrix (numerical gradient), which is computationally expensive.

The time stepping of the vortex particle method is achieved using an low storage 3rd order Runge-Kutta method [58]. This method was suggested by Calabretta due to its low storage requirements relative to traditional Runge-Kutta methods along with the ability to eliminate round-off errors that accumulate over long time simulations [8]. This method has been adopted for the time stepping of vortex particle locations and strengths within the vortex particle method.